2010

A Two degrees-of-freedom (DOF) scanning micromirror using thermocapillary effect in microdroplets

Rakesh Dhull

A Two Degrees-of-Freedom (DOF) Scanning Micromirror Using Thermocapillary Effect in Microdroplets

by

Rakesh Kumar Dhull

A graduate thesis submitted in
partial fulfillment of the requirements for the degree of
MASTER OF SCIENCE
in
Electrical Engineering

Dr. James E. Moon _____ **Date:** _____
(Thesis Advisor)

Dr. Karl D. Hirschman _____ **Date:** _____
(Committee Member)

Dr. David A. Borkholder _____ **Date:** _____
(Committee Member)

Dr. Sohail A. Dianat _____ **Date:** _____
(Department Head)

DEPARTMENT OF ELECTRICAL AND MICROELECTRONIC ENGINEERING
KATE GLEASON COLLEGE OF ENGINEERING
ROCHESTER INSTITUTE OF TECHNOLOGY
ROCHESTER, NEW YORK

October, 2010

Thesis Release Permission Form

Rochester Institute of Technology

Kate Gleason College of Engineering

Title:

A Two Degrees-of-Freedom (DOF) Scanning Micromirror Using Thermocapillary Effect in Microdroplets

I, Rakesh Kumar Dhull, hereby grant permission to the Wallace Memorial Library to reproduce my thesis in whole or part.

Rakesh Kumar Dhull

Date

Dedicated To

My father Sh. Nafe Singh and mother Smt. Chameli Devi.

Beloved brothers Satish, Rajesh, Tajinder and Dinesh.

"असतो मा सद्गमय

तमसो मा ज्योतिर्गमय

मृत्योर्मा अमृतं गमय

ॐ शांति शांति शांतिः"

(Brihadaranyaka Upanishad 1.3.28)

May we find Truth from Falsehood!

May we find Light from Darkness!

May we find the Nectar of Immortality from Death!

Let there be Peace, Peace, Peace!

Acknowledgement

I owe my deepest gratitude to Dr. James Moon for being my mentor, thesis advisor and a role model throughout my tenure in RIT. His personality and dedication towards student understanding of different concepts is unmatched in the academic world. Without his humble guidance, support and help writing this thesis would not be possible.

My sincere thanks to Dr. Karl Hirschman and Dr. David Borkholder for spending their invaluable time and being part of the thesis committee. I am extremely thankful to Dr. Yen-Wen Lu for his help, motivation and valuable discussion.

My special thanks to Dr. Lynn Fuller and Ivan Puchades for their persistent help during the device fabrication and helping me in learning different fabrication tools. I would also like to thank Dr. Sergey Edward Lyshevski for his timely guidance and suggestions. I would like to acknowledge the members of the Semiconductor and Microsystems Fabrication Laboratory (SMFL) for their help and for keeping tools up all day.

I am personally thankful to Bindumadhav Sabnavis, Yusuke Takahashi, Zhonghua Yao, Xiang Li and Michael Pepen, members of Nano and Micro Manufacturing Laboratory (NMML), for their help and memorable time we spent together. I would also like to thank Liang Cao and Karthik Narayanan from Lobezzo Optics Lab for their assistance in optical test setup and valuable discussions.

This research work was partially supported by Texas Instruments/Harvey Award.

Table of Contents

Abstract

This thesis research proposes a novel and simple means of tilting micromirror on a microdroplet by utilizing thermocapillary actuated droplet deformation. Device theory, device design, fabrication, packaging, testing and results are discussed to demonstrate the operation of a 2-degrees-of-freedom (2- DOF) scanning micromirror. Thermocapillary, or Marangoni, effect and contact angle hysteresis are employed to control the droplet shape and position. Hysteresis in different liquids is studied with its influence on the stability of the droplet. The device consists of a micromirror placed onto a microdroplet, and can produce a 6.5° tilting angle when actuated at 30 V. The tilting angle is found to be almost linearly dependent on actuation voltage. Linear, square and circular laser scanning patterns were drawn to demonstrate its successful operation. This technique shows potential applications in scanning micromirror and display technology. Finally, possible future work is discussed to further improve the device performance.

List of Figures

List of Tables

List of Acronyms

MEMS	Micro Electromechanical System
MOEMS	Micro Opto Electromechanical System
DLP	Digital Light Processing
DMD	Digital Micromirror Device
RIE	Reactive Ion Etching
DOF	Degrees of Freedom
EWOD	Electrowetting On Dielectric
CMOS	Complementary Metal Oxide Semiconductor
SRAM	Static Random Access Memory
LPCVD	Low Pressure Chemical Vapor Deposition
LTO	Low Temperature Oxide
PCB	Printed Circuit Board
DI	De-ionized
CCD	Charge Coupled Device
DC	Direct Current
CPLD	Complex Programmable Logic Device
PDMS	Polydimethlysiloxane
PDE	Partial Differential Equation
2-D	Two Dimensional

List of Scientific Constants and Symbols

V	Voltage
η	Dynamic viscosity
μm	Micrometer (10^{-6} meters)
nm	Nanometer (10^{-9} meters)
Å	Angstrom (10^{-10} meters)
θ	Contact angle
υ	Liquid viscosity
σ	Surface tension
$d\gamma$	Surface tension gradient
dc	Concentration of surfactants
E	Electric field
ε	Temperature coefficient of surface tension
γ_{LG}	Liquid-gas surface tension
γ_{SL}	Solid-liquid surface tension
γ_{SG}	Solid-gas surface tension
H	Contact angle hysteresis
R	Droplet radius
R_c	Critical radius
$h(x)$	Droplet shape
U	Droplet velocity
γ_{aLG}	Liquid-gas surface tension at the advancing edge of droplet
γ_{rLG}	Liquid-gas surface tension at the receding edge of droplet
F_t	Threshold stress

δ	Contact angle hysteresis

1 Introduction

The emergence of microfabrication and microelectromechanical systems (MEMS) technology has enabled pathbreaking applications in the fields of science and engineering. Microfabrication involves manufacturing miniature devices on silicon, glass, silicon-on-glass (SOG) and polymer substrates using well-established microelectronics techniques like thin-film growth/deposition, photolithography, dry/wet etching, direct printing and electroplating. MEMS technology employs principles of microfabrication, electronics and mechanics to design and develop novel and sophisticated sensor and actuator devices. Mass production capability, superior immunity to noise and vibrations, miniature size, low cost, high sensitivity and light weight are some of the many inherent advantages that MEMS devices offer compared to their bulk counterparts.

An average human being is using an ever-increasing number of MEMS devices to accomplish his day-to-day work. Accelerometers in cars and cellphones, pressure sensors in automobile tires, humidity and temperature sensors at home, and scanning micromirrors in projectors are some of the MEMS devices that we use every day, knowingly or unknowingly. A number of MEMS devices like gyroscope, inertial sensor and micromirrors are also used for sophisticated technologies like missiles, rockets and satellites navigation and maneuvering.

Lately, micromirror actuation has gained tremendous interest in both industry and academia. Micromirror actuation has widespread applications in the field of telecommunications, display technology, medical equipment, space technology and consumer electronics, to name a few. For example, various kinds of micromirrors manufactured by MEMS fabrication techniques have been demonstrated in the literature. Werber *et al.* [1] used thermal expansion of air inside a cavity to get a micromirror tilt up to 13º. Yoshihata *et al.* [2] used electrostatic forces to deform a parylene-encapsulated microstructure and

tilted a silicon plate by ~1º at 270 V. Elata *et al.* [3] tilted micromirrors suspended on beams, using thermally-induced dipole moment.

Meanwhile, micromirror actuation in *x*-*y* directions can also be used to demonstrate a two degrees-of-freedom (2-DOF) scanning micromirror. The actuation mechanisms for these micromirrors generally resort to electrostatic [4-6], piezoelectric [7], electrothermal [8], electromagnetic [9-11], thermo-pneumatic [1], and temperature gradient [3] techniques. However, micromirror devices based on these mechanisms often require complex microfabrication processes, containing beam or hinge structures, which suffer from mechanical degradation, due to contact or torsion.

To address these issues, micromirror actuation in conjunction with microfluidics has gained commendable interest recently. For instance, electrowetting based droplet actuation is exploited to control the micro-object movement and to show its potential in piston-motion micromirror applications [12]. Microscale droplet manipulation has been widely employed in microfluidics and lab-on-a-chip development, where microdroplets are often used to transport and mix small volumes of fluids in biological and chemical sample processing [13-16]. Two major methods utilized for droplet manipulation are the use of electrowetting and thermocapillary effects [16-18]. Meanwhile, thermocapillary forces due to the low actuation voltages have drawn great attention in the microfluidic applications [17-18].

To implement a simple mechanism and fabrication technique, as well as to have a low voltage for micromirror actuation, our device exploits the thermocapillary effect, also called Marangoni effect, to create convection flow inside a droplet, inducing the droplet deformation to tilt the micromirror on the top. More importantly, contact angle hysteresis is utilized to prevent the droplet from rolling out of its position and to stabilize the device.

----------x----------x----------x----------

2 Motivation and Background

The motivation for this research was Texas Instruments Digital Light Processing (DLP) technology, which employs millions of micromirrors laid out in a matrix on a semiconductor chip, also known as a Digital Micromirror Device (DMD) [19-22]. State of the art chip these days employs up to 2 million hinge-mounted micromirrors. Each pixel on the projected screen is represented by a single micromirror on the DMD chip. Therefore, the number of mirrors determines the resolution of the DLP projector. Figure 2.1 shows an exploded view of a single CMOS SRAM memory cell together with a micromirror, on a DMD chip. CMOS memory cell is used for independently addressing and controlling each micromirror on the chip.

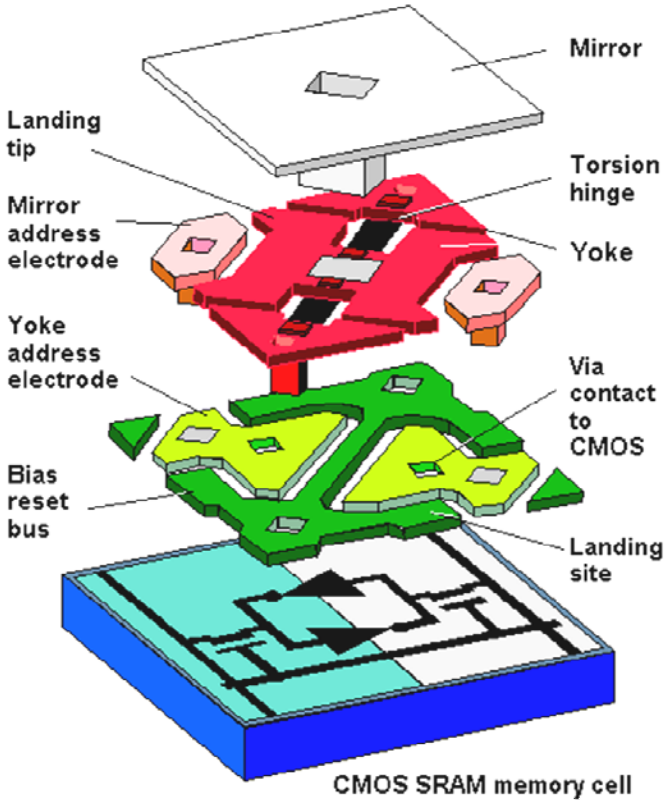

Figure 2.1: The detailed view of an individual CMOS SRAM memory cell with a micromirror structure on top, used in Texas Instruments Digital Light Processing (DLP) technology [21] (permission requested).

Each micromirror is actuated due to the generation of electrostatic force between the mirror-addressed electrode and the yoke addressed electrode, as shown in Figure 2.1. Typical micromirror tilt obtained is ± 10° which corresponds to ON and OFF states, when voltage is applied to the underneath electrodes as shown in Figure 2.2. This produces a light and dark pixel on the projected screen. Different gray shades are generated corresponding to different actuation frequencies of the micromirrors. A light gray pixel is generated when a micromirror is switched ON more frequently than OFF, and a darker gray pixel is created when micromirror is switched OFF more frequently. The DLP chip micromirrors have a frequency response of up to 5 kHz.

A DLP chip can project up to 1,024 shades of gray pixels, thus projecting a high resolution grey image. Subsequently, to add color, white light from a source is passed through a color filter as it reaches the DLP chip surface as shown in Figure 2.3. This filters the light into a minimum of red, green, and blue, thus creating at least 16.7 million colors from a single DLP chip. DMD technology requires a complex fabrication process; however, once fabricated they have been tested to operate even after 1 trillion cycles.

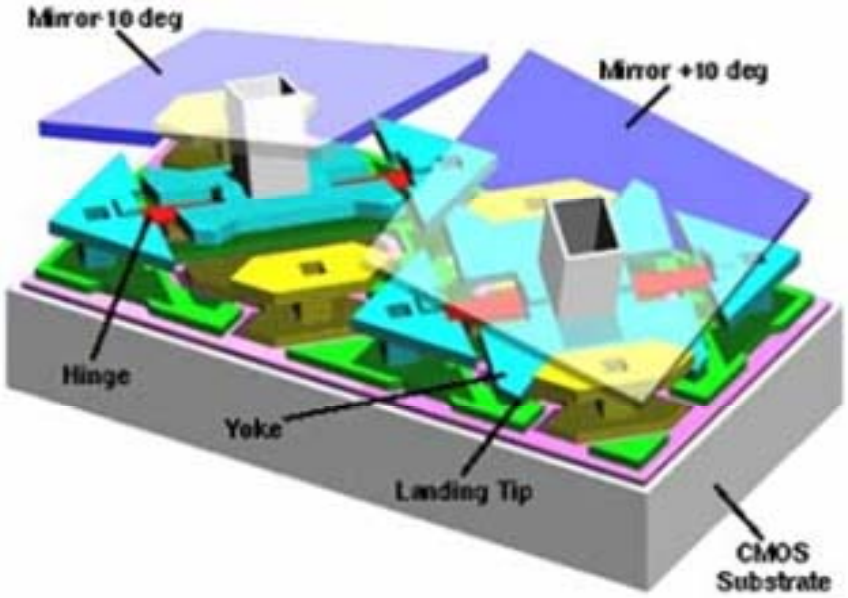

Figure 2.2: The schematic of micromirror actuation on a DMD chip. Micromirror can be tilted ± 10° when actuation voltage is applied to the underneath electrodes [22] (permission requested).

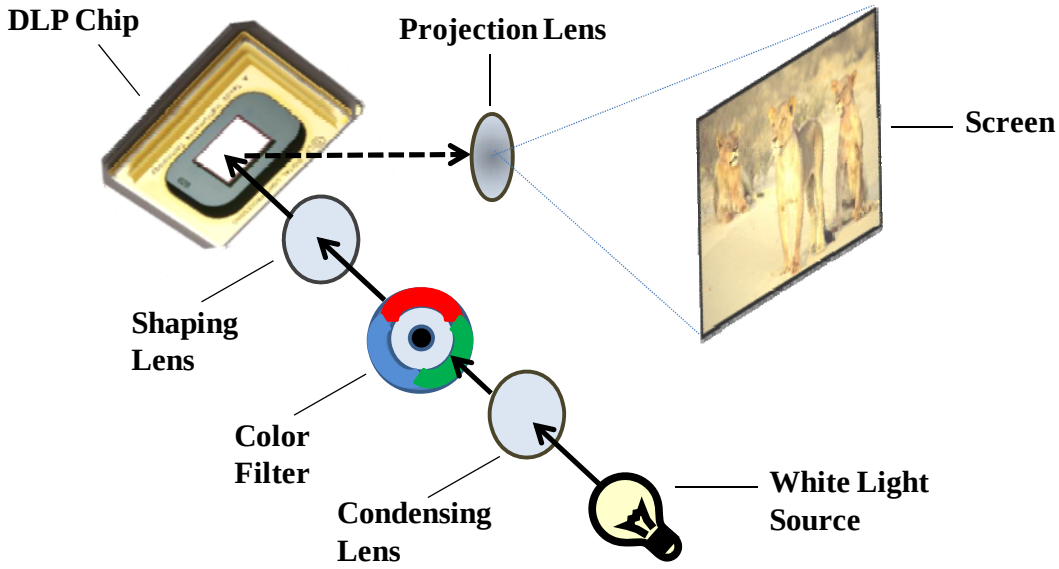

Figure 2.3: The schematic of a colored picture generation using a DMD chip. An RGB color filter wheel is used along with optics to project the screen (adapted from [23]).

Subsequently, to get further ideas about research and development in the field of micromirror actuation, different kinds of micromirror actuation techniques were studied. For example, Figure 2.4(a) shows micromirror actuation employing vertical comb drive actuators, which works on the principle of electrostatic force [4]. Micromirror tilt angles from 4° at low frequencies to 40° at resonance are obtained at an applied voltage of 75 V_{pp}. Resonance frequencies ranged from 5 kHz to 15 kHz, making it suitable for scanning and switching applications. Werber *et al.* [1] showed micromirror actuation using thermo-pneumatic expansion of air inside a cavity as shown in Figure 2.4(b).

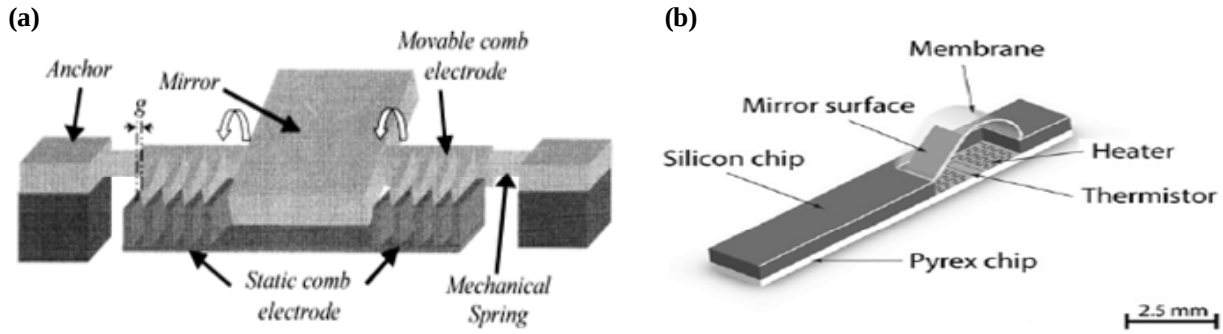

Figure 2.4: The schematic of micromirror actuation techniques. (a) Micromirror tilting using vertical comb drive actuators after permission [4] (after permission), (b) Micromirror tilting on a deformable membrane using thermo-pneumatic pressure generation inside an air cavity [1] (with permission).

The authors fixed micromirrors to a highly elastic membrane, and the microcavity air is heated using built-in microheaters, causing the membrane to expand, thus tilting the micromirror. They successfully demonstrated tilt angles up to 13° with a stroke distance from 0 to 80 μm. A 30 V actuation voltage is applied to get a tilt of approximately 13°. Since heating and cooling of cavity air is a relatively slow process, the limitation of this technique is the low frequency response of device (frequency response ~ 10 mHz).

In an another paper, Yoshihata *et al.* [2] demonstrated a scanning micromirror using deformation of a parylene-encapsulated liquid structure (PELS). Silicone fluid is used as an encapsulated liquid between a silicon plate and an electrode-patterned structure as shown in Figure 2.5. Gold is used for the upper electrode and aluminum for the base electrode. When voltage is applied to the two electrodes, electrostatic force causes the parylene structure to deform, hence tilting the top silicon plate as shown in Figure 2.5. A typical micromirror tilt angle of 1° is obtained at 270 V actuation voltage. The limitation of this device is low tilt angles and high actuation voltage requirement. Furthermore, the fabrication process seems to be highly complex, requiring extreme care.

Another interesting technique to tilt a micromirror is demonstrated by Kang *et al.* [24] using an electrowetting-on-dielectric (EWOD) method. Figure 2.6 consists of a micromirror placed on top of four water microdroplets. When the voltage is applied, electric potential across the liquid-solid interface changes the wettability due to charge redistribution, causing the contact angle of droplets to change. This effect has been utilized in this paper to tilt micromirror on top of four microdroplets. A 4° micromirror tilt is demonstrated at 90 V actuation voltage at 15 Hz frequency. The drawback of this technique is the requirement of high actuation voltage and low tilt angles. Additionally, the device does not look stable since water microdroplets evaporate very fast even at room temperature.

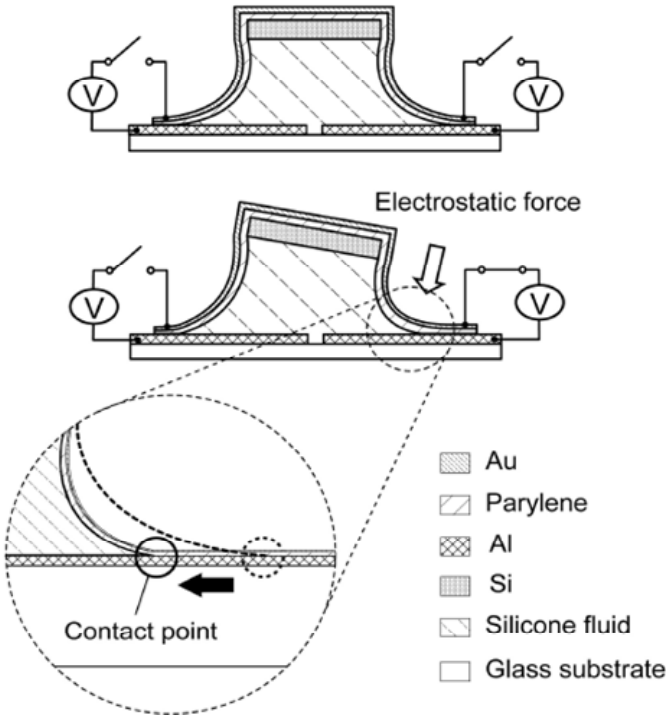

Figure 2.5: The schematic of silicon plate tilting using parylene-encapsulated liquid structure (PELS) by generating electrostatic force between gold and aluminum electrodes [2] (with permission).

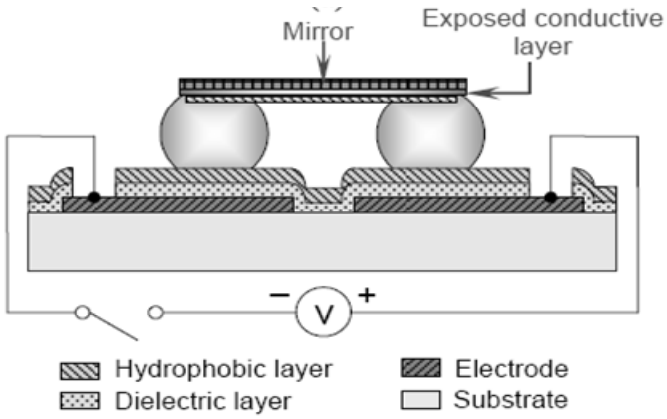

Figure 2.6: Micromirror tilting on top of four water microdroplets using electrowetting-on-dielectric (EWOD) technique [24] (with permission).

----------x----------x----------x----------

3 Device Theory

The device reported in this thesis works on the principle of thermocapillary effect, or Marangoni effect, where the gradient of surface tension due to temperature variation causes liquid to flow away from the regions of low surface tension. Thermocapillary effect results due to the variation of interfacial surface tension at a liquid-liquid interface caused by temperature differences [18]. Meanwhile, the surface tension gradient ($d\gamma$) can also be caused by concentration of surfactants (c), and even by an electric field (E) [25] as expressed by eq. (3.1)

$$d\gamma = \frac{\partial \gamma}{\partial T} dT + \frac{\partial \gamma}{\partial c} dc + \frac{\partial \gamma}{\partial E} dE, \tag{3.1}$$

where γ is the surface tension of liquid and T is the liquid temperature. However, this device utilizes only temperature to create the required surface tension gradient. It is important to mention here that thermocapillary effect depends on temperature gradient rather than temperature alone.

3.1 Understanding Contact Angle

To better understand the thermocapillary effect, it is significant to understand the contact angle and surface tension at solid-liquid-gas interfaces. Figure 3.1 shows the schematic of a liquid droplet on a flat homogeneous solid surface with and without the influence of any force applied.

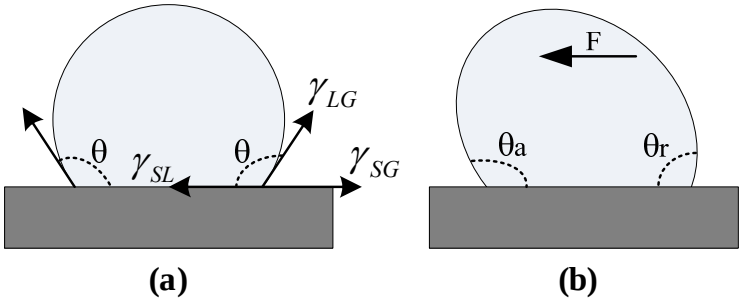

Figure 3.1: The schematic of contact angle and surface tension at solid-liquid-gas interfaces for a liquid droplet on a solid surface: (a) Equilibrium contact angle with no force applied. (b) Force F induces advancing and receding angles inside a droplet.

The contact angle of a droplet is the equilibrium angle that a liquid meniscus makes with a solid surface as a consequence of surface tensions at the solid, liquid and gas interfaces as shown in Figure 3.1(a). It can be further expressed by Young's equation (eq. 3.2)

$$\gamma_{LG}\cos(\theta)+\gamma_{SL}=\gamma_{SG}, \tag{3.2}$$

where θ is the droplet contact angle, γ_{LG} is the liquid-gas surface tension, γ_{SL} is the solid-liquid surface tension and γ_{SG} is the solid-gas surface tension. Furthermore, equilibrium contact angle can be represented as in eq. (3.3)

$$\theta=\cos^{-1}\left[\left(\gamma_{SG}-\gamma_{SL}\right)\Big/\gamma_{LG}\right]. \tag{3.3}$$

The contact angle of a droplet also provides the inverse measure of surface wettability. A surface is considered favorable for wetting if the contact angle is less than 90º, whereas it is considered unfavorable if contact angle is greater than 90º. As can be seen from Figure 3.1(b), the droplet deforms under the influence of force *F*, creating advancing (θ_a) and receding (θ_r) angles. It is important to mention here that the contact angles shown in Figure 3.1 are just for theoretical demonstration and may not comply with contact angles of mustard oil droplet in our experimentation.

Additionally, when a droplet deforms, the advancing angle is always greater than the receding angle and the droplet always deforms and moves in the advancing angle direction. For interested readers, the two different approaches used to measure advancing and receding angles in a droplet are discussed in detail in Appendix A.

3.2 Thermocapillary Effect

For the case of thermocapillary effect in droplets, liquid flow from a hot region towards a cold region exerts Marangoni force on the droplet, creating advancing and receding angles as shown in Figure 3.2.

For a small temperature range, the liquid surface tension (σ_{lv}) decreases linearly with temperature and can be described mathematically as in eq. (3.4)

$$\sigma_{lv}(T) = \sigma_{lv0} - \varepsilon\left(T - T_0\right), \tag{3.4}$$

where σ_{lv0} is the liquid-vapor surface tension at room temperature, ε is the temperature coefficient of surface tension, T is the liquid temperature and T_0 is the room temperature. Therefore, the liquid in the warmer region is pulled towards the colder region, where the surface tension is higher, to minimize the total surface energy. The liquid flow inside the droplet exerts a hydrodynamic force on the solid surface in the direction of applied temperature gradient. As a result, the solid immobile surface exerts an equal and opposite force on the droplet, causing droplet deformation [18]. Hence, temperature gradient ($\Delta T = T^+ - T^-$) can be utilized to change droplet shape and to demonstrate droplet actuation.

It is interesting to note that the liquid flow inside the droplet in Figure 3.2(a) and Figure 3.2(b) are directly opposite to each other due to the different position of microheaters. Since the microheater in Figure 3.2(a) is directly below the microdroplet, it causes liquid to flow in clockwise direction. This happens because convective heat flows from the center towards the surface of the droplet. Whereas, for the case of microheater away from the droplet liquid moves in the counter-clockwise direction. This is due to the transfer of heat from the surface of the droplet towards the centre.

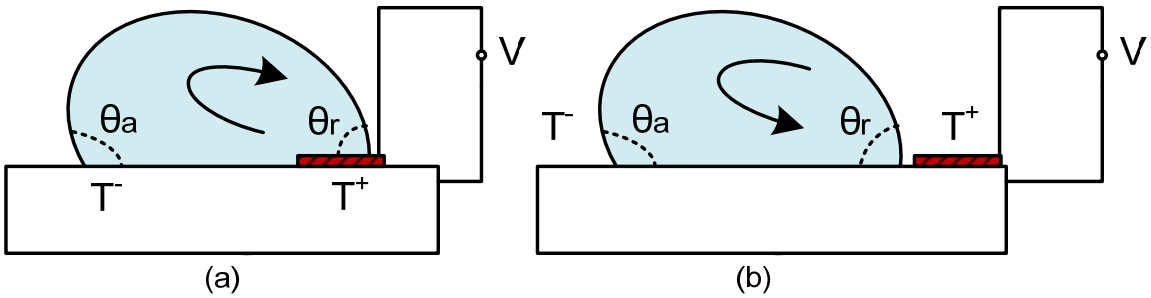

Figure 3.2: The schematic of thermocapillary actuation or Marangoni effect. Liquid moves from the hot (T^+) to the cold (T^-) side on a hydrophobic substrate. (a) Liquid inside the droplet flows in clockwise direction. (b) Liquid inside the droplet moves in counter-clockwise direction.

Meanwhile, proper operation of this device requires a hydrophobic surface with good droplet contact angles. Since oils are extremely hydrophilic towards silicon, Teflon© AF 1600 is spin-coated to make a hydrophobic surface, thus increasing the contact angle of the droplet. The contact angle of mustard oil is found to be 82.4° and 32° with and without Teflon layer, respectively. Polysilicon microheaters were fabricated to create the required temperature and surface tension gradients, causing the liquid flow and thus changing the droplet shape. According to the thermocapillary effect, the droplet advancing angle increases (θ_a) and the receding angle (θ_r) decreases when increasing voltage is applied to the polysilicon microheaters.

3.3 Contact Angle Hysteresis

The difference between the maximum advancing angle and the minimum receding angle of the droplet determines the contact angle hysteresis (H), as expressed in eq. (3.5) [26]

$$H = \left[\max(\theta_a) - \min(\theta_r)\right] \tag{3.5}$$

This hysteresis is the measure of the droplet's resistance to any motion and determines the stability of device. The larger the contact angle hysteresis, the greater is the force required to move the liquid meniscus and the droplet from its current position. Therefore, selecting the right liquid and substrate is a crucial task for better device performance. Table I shows various liquids with their viscosity, contact angle and hysteresis factor.

As can be seen from Table I, mustard oil (allyl isothiocyanate) has high viscosity, good contact angle on Teflon and high hysteresis factor, which makes it the best liquid choice for device testing [27]. Although large contact angle hysteresis is preferable, as explained earlier, other considerations are also needed to optimize the device performance. For instance, deionized **(**DI) water shows high hysteresis, but it has evaporation problems due to the heat application. In addition, high-viscosity liquids show little internal convection, but provide a better stability to hold the mirror; whereas low-viscosity liquids are often agitated by convective motions easily. Mustard oil, or allyl isothiocyanate, is chosen for better

device stability and performance. This is due to its large hysteresis, high viscosity, and lower vapor pressure, thus, eliminating the evaporation problem as seen otherwise in aqueous-solution-based actuation devices.

Table I: Liquid selection for the thermocapillary device and their properties (from measurement).

Liquid	Viscosity (Pa·s @ 25°C)	Contact angle on Teflon©	Contact angle hysteresis *(H)*
Mustard oil	70	82.4°	4.6°
Silicone oil	9.3×10^{-3}	51.4°	3.2°
Glycerin	1.5	108.5°	4.5°
DI water	8.9×10^{-4}	120°	5.5°

3.4 Understanding Droplet Dynamics

Meanwhile, Chen *et al.* [26] have developed a steady-state model that explains the droplet velocity and used it to find out the threshold stress required for droplet motion. Their model provides an excellent understanding of the relationship among liquid surface tension, applied temperature, advancing and receding contact angles. The schematic of the droplet geometry and actuation is shown in Figure 3.3. Various assumptions made to implement the model are discussed below:

i. The model is solved within the lubrication approximation considering a Newtonian liquid.

ii. The droplet is moving at a constant velocity U in response to a positive thermocapillary stress.

iii. $\frac{d\gamma_{LG}}{dT} >> \frac{d\gamma_{SL}}{dT}$ and $\frac{d\gamma_{LG}}{dT} >> \frac{d\gamma_{SG}}{dT}$

iv. $\frac{d\gamma_{LG}}{dT}$ remains constant for the range of interest.

v. Slip length b is orders of magnitude smaller than local droplet thickness $h(x)$, which is a valid assumption except at droplet edges.

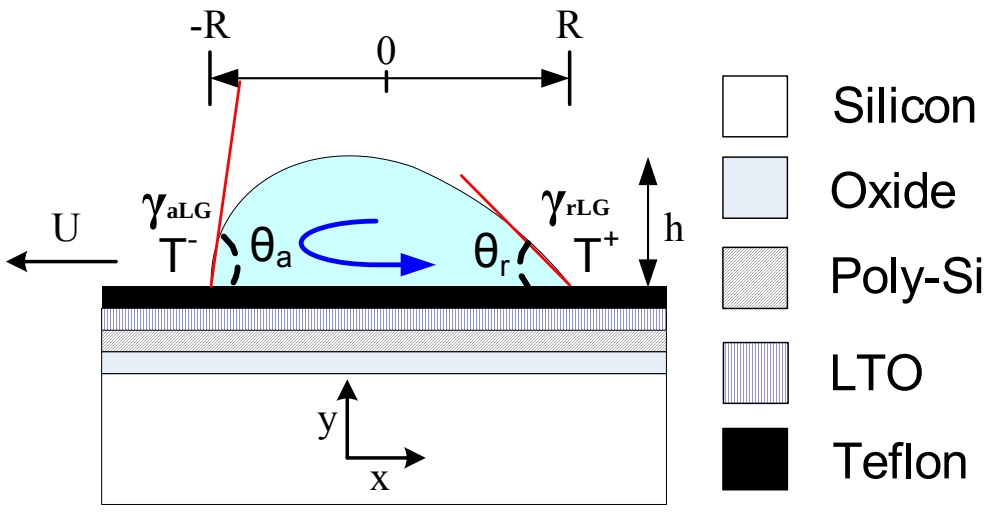

Figure 3.3: The schematic of the droplet actuation under the influence of temperature gradient. Liquid moves from the hot (T^+) to the cold (T^-) side on a hydrophobic substrate.

Using this model, velocity of the droplet can be expressed by eq. (3.6)

$$U = \frac{1}{6\nu J}\left[\left|\frac{d\gamma_{LG}}{dT}\right|\frac{\Delta T}{2R} + \frac{\gamma_{aLG}\cos\theta_a - \gamma_{rLG}\cos\theta_r}{R}\right], \tag{3.6}$$

where v is the liquid viscosity, R is the droplet radius, γ_{aLG} is the liquid-gas surface tension at the advancing edge of droplet, γ_{rLG} is the liquid-gas surface tension at the receding edge of droplet. Furthermore, J is defined as in eq. (3.7)

$$J = \frac{1}{2R}\int_{-R}^{R}\frac{dx}{h(x)+3b} \tag{3.7}$$

where $h(x)$ is the droplet shape and b is the Navier slip length. Since we know that the surface tension is a linear function of temperature γ_{aLG} can be expressed by eq. (3.8)

$$\gamma_{aLG} = \gamma_{rLG} + \left(\Delta T\left|\frac{d\gamma_{LG}}{dT}\right|\right). \tag{3.8}$$

Using eq. (3.8) velocity of the droplet can be expressed by eq. (3.9)

$$U = \frac{1}{6\nu J}\left[\left(1+2\cos\theta_a\right)\left|\frac{d\gamma_{LG}}{dT}\right|\frac{\Delta T}{2R} - \frac{\gamma_{rLG}\left(\cos\theta_r - \cos\theta_a\right)}{R}\right]. \quad (3.9)$$

Therefore, droplet movement depends on the contest between thermocapillary stress and contact angle hysteresis. Since our device works on droplet deformation without any droplet motion, setting $U = 0$ provides the threshold stress required to move the droplet as expressed in eq. (3.10). Therefore, eq. (3.10) can be used to study the pinning down of a droplet in the center of the chip.

$$F_t = \left(\left|\frac{d\gamma_{LG}}{dT}\right|\frac{\Delta T}{2R}\right)R = \frac{\gamma_{rLG}\left(\cos\theta_r - \cos\theta_a\right)}{1+2\cos\theta_a} = \frac{\gamma_{aLG}\left(\cos\theta_r - \cos\theta_a\right)}{1+2\cos\theta_r}. \quad (3.10)$$

As discussed earlier a higher hysteresis is required as it minimizes the droplet linear motion. Meanwhile, the droplet motion can be further prevented with proper selection of the liquid surface tension, droplet diameter and applied voltages, thus contributing only to droplet actuation. Additionally, Brzoska *et al.* [28] have demonstrated that for the onset of droplet motion there exists a critical droplet radius R_c as expressed by eq. (3.11)

$$R_c \approx \frac{\gamma_{LG}}{\theta}\frac{\delta}{\left(\frac{d\gamma_{LG}}{dT}\right)}\left(\frac{dT}{dx}\right)^{-1}. \quad (3.11)$$

Furthermore, δ is an another form of representing contact angle hysteresis which can be expressed as in eq. (3.12)

$$\delta = \cos\left(\theta_a\right) - \cos\left(\theta_r\right). \quad (3.12)$$

As obvious from eq. (3.11), the critical droplet radius depends on temperature and surface tension however, independent of liquid viscosity. However, once this critical radius is achieved the droplet velocity is linearly proportional to the applied temperature gradient and inversely proportional to the liquid viscosity.

Furthermore, viscosity of the liquid depends on the temperature at the center of the droplet and can be expressed as in eq. (3.13)

$$\nu = \nu_0 \exp\left[3.8 T_b \left(\frac{1}{T_c} - \frac{1}{T_0}\right)\right], \tag{3.13}$$

where ν_0 is the viscosity of liquid at room temperature T_0, T_b is liquid boiling point and T_c is the temperature at the center of the droplet [29]. In addition, it is demonstrated that the droplet velocity is minimized if the droplet diameter is approximately 2 mm [28]. This research utilizes this phenomenon for the pinning down of the microdroplet.

Utilizing Marangoni convection and contact angle hysteresis our mechanism of the mirror actuation is illustrated in Figure 3.4. Initially, the micromirror is resting horizontally on a spherically-capped oil microdroplet without any Marangoni flow, when no voltage is applied to the microheaters, as shown in Figure 3.4(a). However, when the voltage is applied, the microheater locally raises the temperature of the droplet, causing the hot liquid (T^+) to move towards the colder region (T^-). Thus, the Marangoni flow introduced inside the droplet deforms the droplet and tilts the micromirror on top, as depicted in Figure 3.4(b).

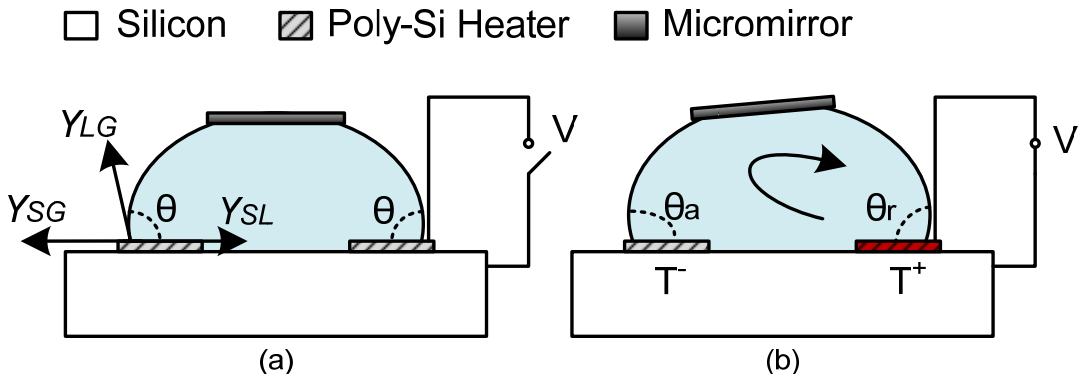

Figure 3.4. The schematic of micromirror tilting on a hydrophobic substrate. (a) Micromirror resting on the oil droplet without any actuation voltage applied. (b) Liquid moves from the hot (T^+) to the cold (T^-) region on a hydrophobic substrate when actuation voltage is applied to the right microheater. Micromirror is tilted due to the droplet shape deformation.

----------x----------x----------x----------

4 Device Design

The layout of the device is designed using Mentor Graphics software and requires a total of four mask layers as shown in Figure 4.1, namely: poly, contact, metal and Teflon. The device design consists of four polysilicon heaters making a donut shape as numbered 1, 2, 3 and 4 in Figure 4.1. Polysilicon microheaters are designed in a circular shape to completely cover the droplet circumference. Therefore, these microheaters also define a circular area for placing the microdroplet on top of the chip. Outer circumference and inner circumference of each microheater are measured 2 mm and 1.25 mm respectively. Each microheater area is measured to be approximately 0.825 mm^2. Voltage can be applied to each microheater independently, thus heating one-fourth of the droplet volume.

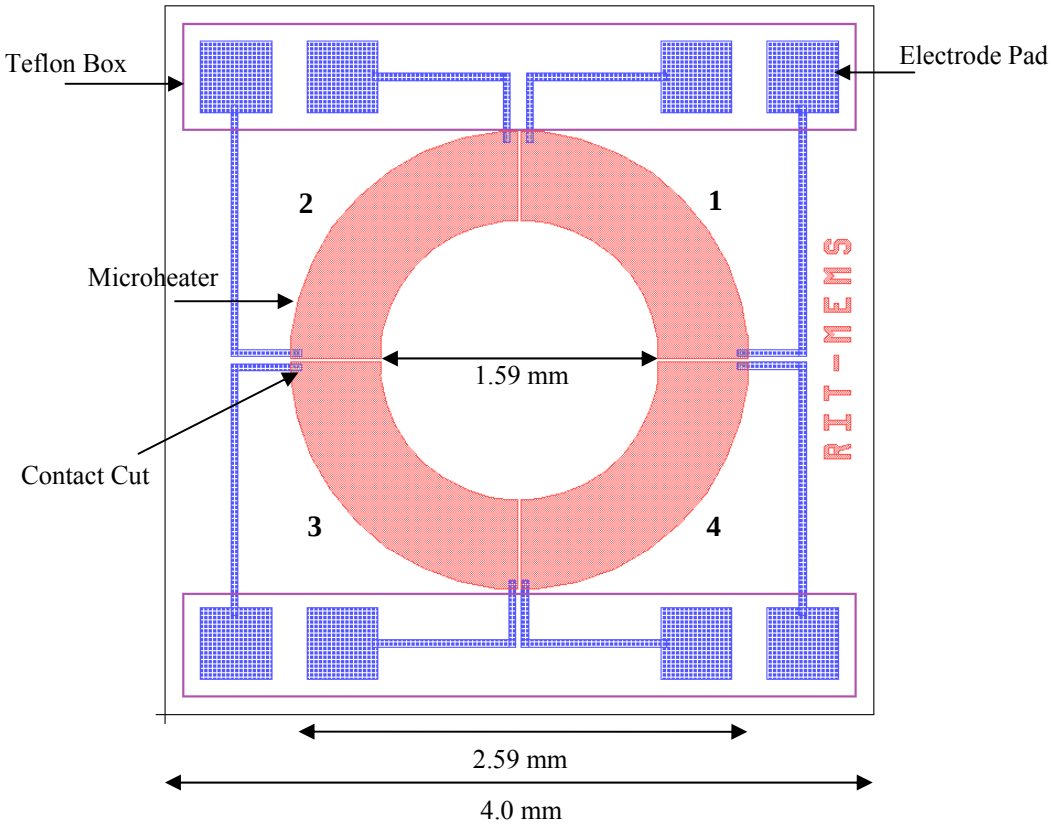

Figure 4.1: Layout of the device showing polysilicon microheaters (1, 2, 3 and 4), and metal electrodes. Teflon is coated, except in the "Teflon box" regions.

Each microheater is connected with two electrodes for applying actuation voltage. Contact cuts are designed to connect metal pads with polysilicon microheaters. Finally, the “Teflon box” defines the region where hydrophobicity, or Teflon layer, is not required.

After the successful fabrication, operation and testing of the device in Figure 4.1, different layouts were generated. Various designs were used for testing the device and micromirror actuation using different shape and size polysilicon microheaters and actuation schemes. For example, Figure 4.2(a) shows the device design with smaller size microheaters. A smaller droplet on these microheaters ensures faster liquid heating and improved droplet actuation. The layout in Figure 4.2(b) is designed to employ four microdroplets supporting a single micromirror on top. As shown, each resistor can heat one-half of the droplet volume. Smaller droplet volume would further increase the droplet deformation, causing higher micromirror tilt angle. Furthermore, the design in Figure 4.2(c) was drawn to test the vertical actuation of the droplet. The Figure 4.2(d) design was implemented to test the operation of a liquid micromotor. This design was specifically made for rotating the micromirror on the droplet, thus acting as a liquid micromotor. Similarly, various other designs were drawn which have not been discussed here.

Finally, all the designs were assembled to make a 5 x 5 matrix (as shown in Figure 4.2(e)) which is repeated to produce the final mask layout as shown in Figure 4.2(f). Alignment marks and critical dimension structures employed for the proper alignment of different layers are shown in Figure 4.2(g). A level 1 alignment mark scheme was used during the fabrication of the devices. Finally, GDSII files were generated for each mask layer and sent to Photosciences for fabrication on a 5 x 5 x .090 inch sodalime glass with chrome masking material.

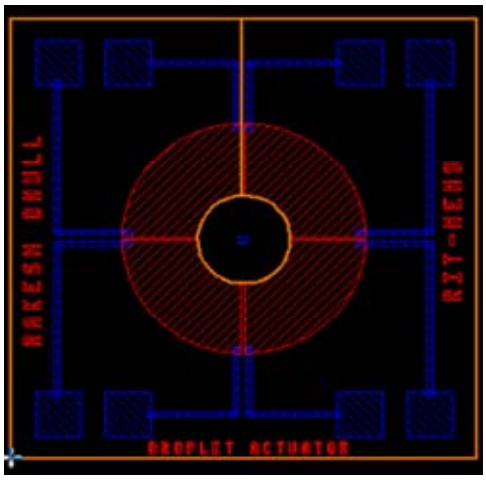
RAKESH DHULL
RIT-MEMS
DROPLET ACTUATOR

(a)

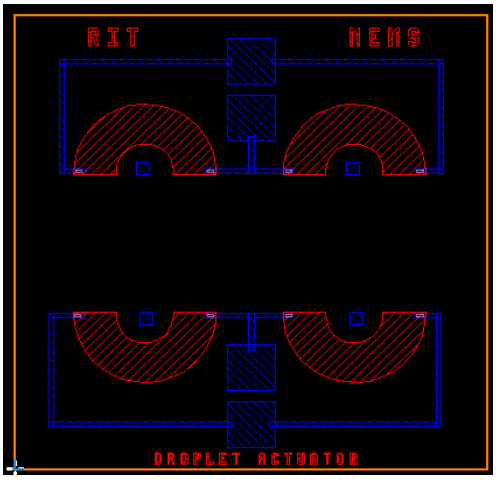
RIT
MEMS
DROPLET ACTUATOR

(b)

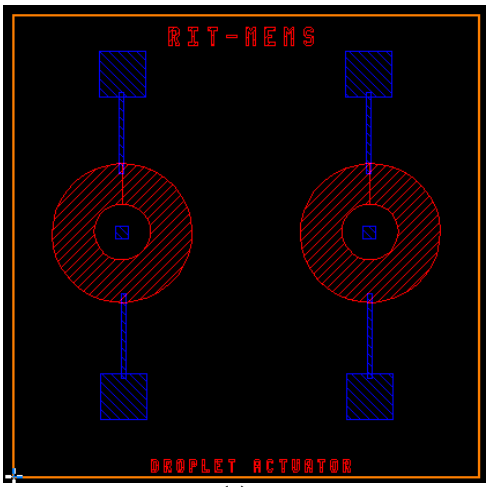
RIT-MEMS
DROPLET ACTUATOR

(c)

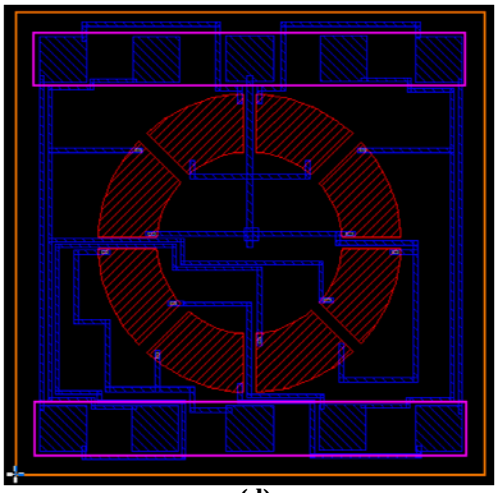

(d)

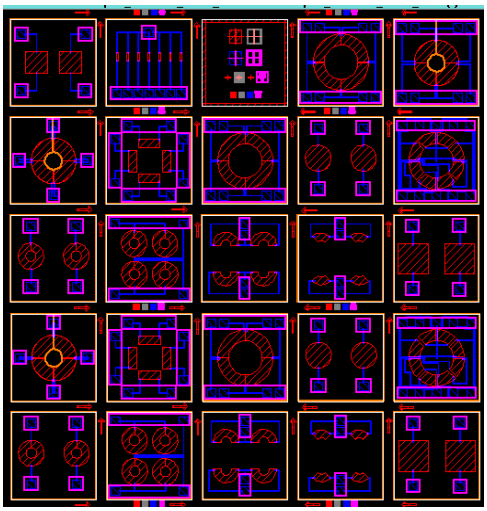

(e)

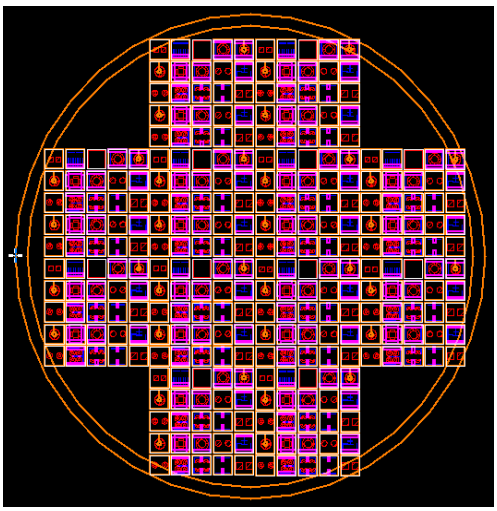

(f)

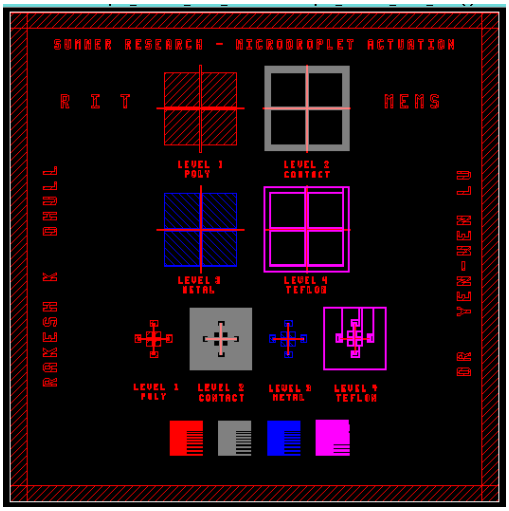

(g)

Figure 4.2: Designs: (a) Smaller polysilicon heater design to place a smaller droplet for increasing the Joule heating and droplet actuation. (b) Four microdroplets for supporting a micromirror. (c) Vertical actuation of the microdroplets. (d) Layout for a liquid micromotor. (e) 5 x 5 cell of different designs used for making mask layout. (f) Final mask layout by repeating cell shown in figure 4.2(e). (g) Alignment marks and critical dimension structures used for layer alignments.

----------x----------x----------x----------

5 Device Simulation

Numerical calculations were conducted to evaluate the device performance and to explore the steady-state analysis of the Marangoni flow or liquid flow inside the droplet. The simulations were performed by employing Incompressible Navier-Stokes, Convection and Conduction and Weak Form, Boundary application modes in the Comsol© software. The main objective of performing simulation was to understand the different liquid flows, liquid flow directions and velocity vectors inside the droplet. This was important as it provided better understanding of droplet actuation and micromirror tilting. Some constants used during the simulation which will be used in the following sections are shown in Figure 5.1.

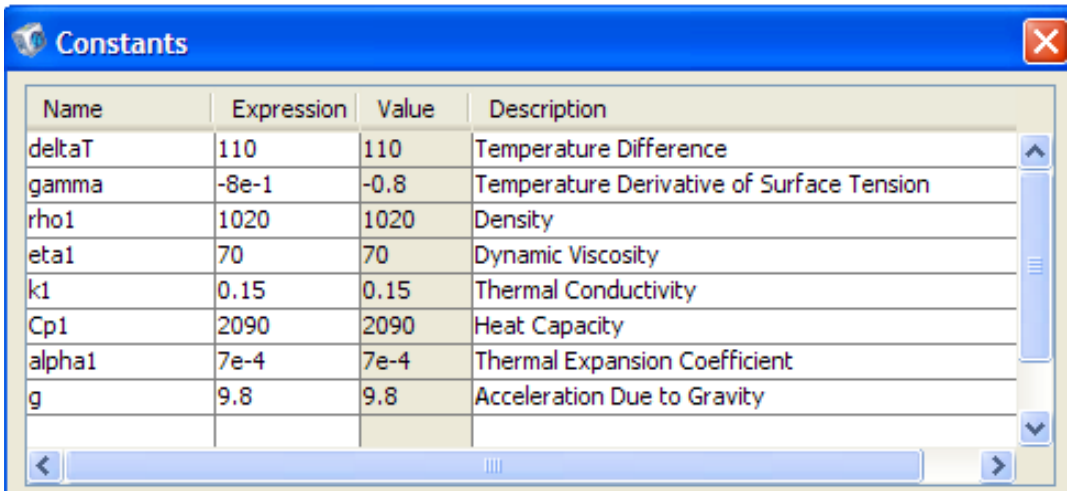

Figure 5.1: The different constants used during simulation in Comsol© software.

5.1 Model Design

A 2-D mustard oil droplet model with a microheater underneath is shown in Figure 5.2. The droplet diameter is set to be 2 mm with an approximate height of 0.65 mm. The contact angle of droplet is designed to match approximately the contact angle of actual oil droplet during the device operation. Since the height of droplet is much larger than the thickness of microheater, our simulation model neglects the

effect of topography on droplet actuation. The simulation boundary shown in Figure 5.2, describes the outer peripheries of the simulation model.

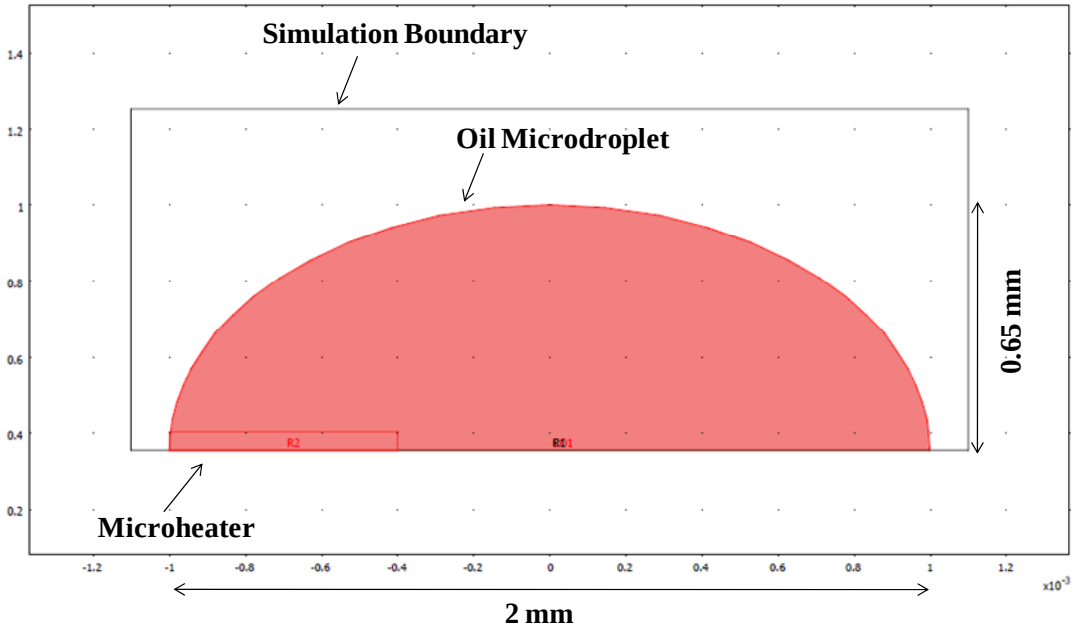

Figure 5.2: Model of the microdroplet on top of a microheater for simulating convective flow inside the droplet. Model designed using Comsol© software.

5.2 Model Meshing

Subsequently, the droplet model was meshed using a fine triangular meshing scheme. The meshed model is shown in Figure 5.3. The maximum element size for meshing is set to be 4e-5 and solved with 47520 degrees of freedom.

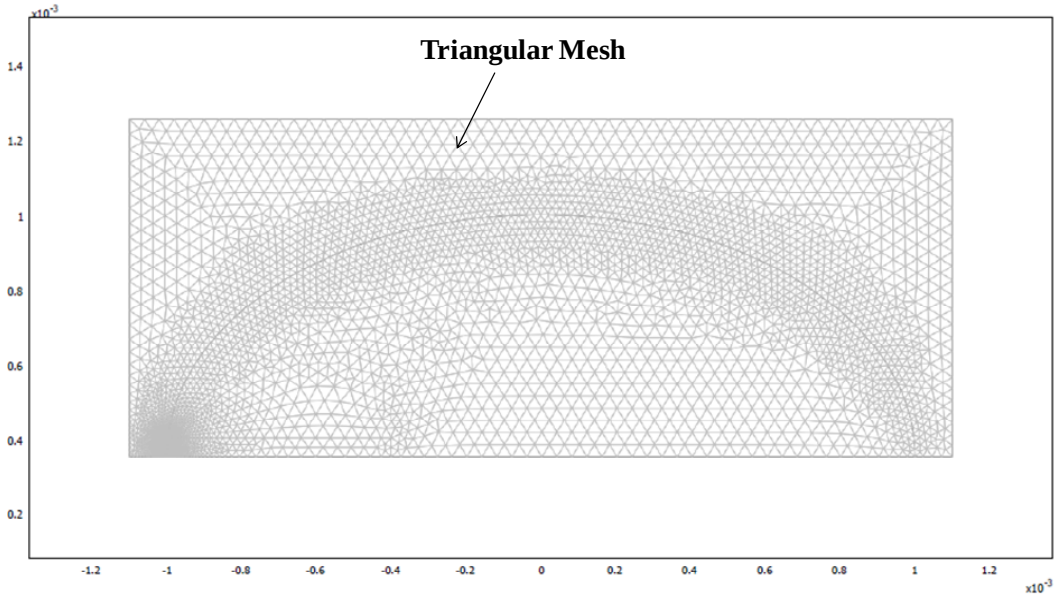

Figure 5.3: The triangular meshed model of a droplet on top of a microheater. Meshing performed using Comsol© software.

5.3 Incompressible Navier-Stokes Model

An Incompressible Navier-Stokes application mode with no-slip boundary condition was used in Comsol© to simulate the liquid flow inside the droplet.

5.3.1 Boundary Conditions

The different boundaries selected for correctly simulating the model are shown in Figure 5.4. Furthermore, Table II demonstrates the different boundary types and boundary conditions used for liquid momentum balance. As obvious from Figure 5.4 and Table II, B1 and B2 represent the boundaries where droplet is sitting on top of the microheater. Similarly, boundary B3 represents where droplet is touching the chip surface. Therefore, B1, B2 and B3 are all set as wall with no-slip boundary condition. In addition, B4 and B5 represent boundaries between the droplet and the ambient environment. A symmetry boundary type is used to establish no penetration and vanishing shear stresses across the liquid-air interface.

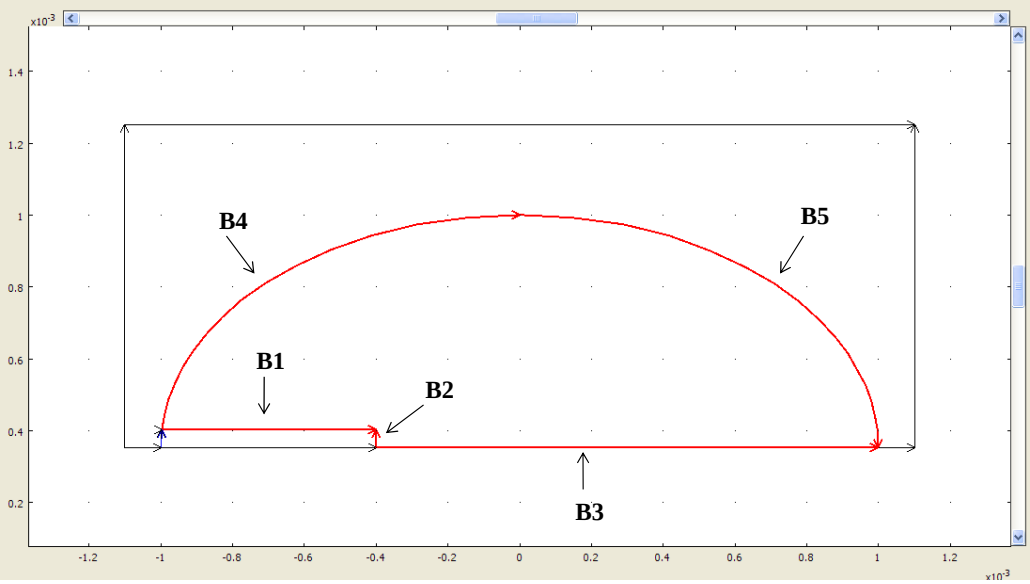

Figure 5.4: Various boundaries used for implementing Incompressible Navier-Stokes application mode in Comsol© software.

Table II: Boundary conditions used for Incompressible Navier-Stokes application mode in Comsol© simulation.

Settings	B1	B2	B3	B4	B5
Boundary Type	Wall	Wall	Wall	Symmetry Boundary	Symmetry Boundary
Boundary Condition	No Slip	No Slip	No Slip	-	-

5.3.2 Subdomain Settings

The subdomain settings are used to define the physics on a model's domain, which is divided into different subdomains. For the Incompressible Navier-Stokes application mode subdomain S1 is defined as a mustard oil liquid droplet as shown in Figure 5.5. Table III shows various settings used for defining density, dynamic viscosity and volume force in y-direction for the S1 subdomain.

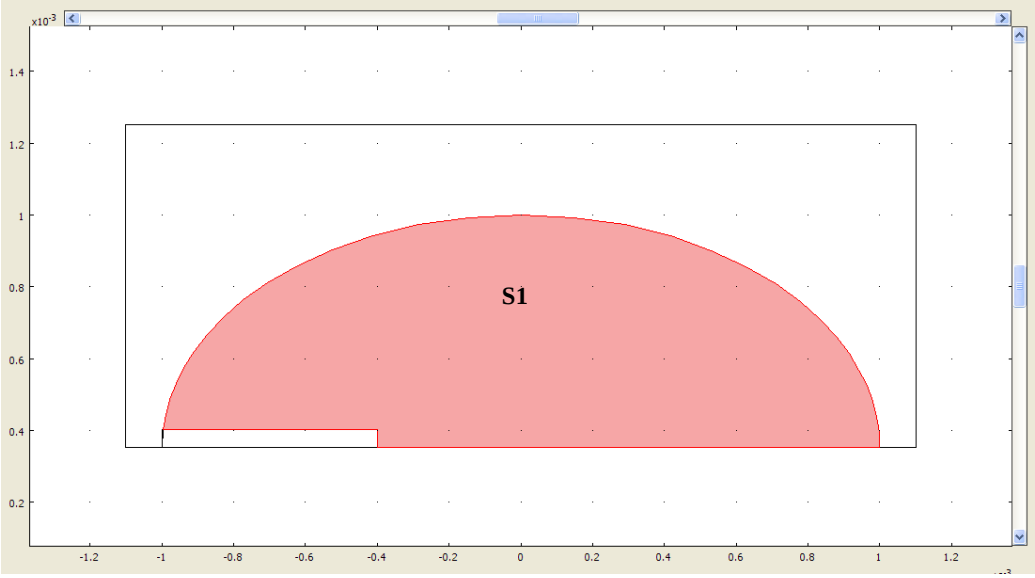

Figure 5.5: Subdomain used for Incompressible Navier-Stokes model in Comsol© software.

Table III: Subdomain settings used for Incompressible Navier-Stokes application mode in Comsol© simulation.

Settings	S1
Density	rho1
Dynamic Viscosity	eta1
Volume Force in y-direction	alpha1* g * rho1* (T - deltaT/2)

5.4 Convection and Conduction Model

Convection and conduction application mode was used to take heat flow inside the droplet into account.

5.4.1 Boundary Conditions

The different boundaries selected for simulating the Convection and Conduction model are shown in Figure 5.6. Table IV demonstrates the different boundary types and boundary conditions used for convective heat transfer inside the fluid. As obvious from Figure 5.6 and Table IV, B1, B3 and B4 represent the microheater boundaries and are set to *deltaT* (ΔT). Since the fabricated device has a 0.5 µm thick oxide layer below the polysilicon microheater, it is fair to assume that heat loss through the bottom

part of chip is negligible. Henceforth, boundaries B2, B7, B8 and B12 are set as thermal insulation. Similarly, boundaries B9, B10 and B11 are also set to thermal insulation by assuming that there is no heat loss outside the model periphery. Since B5 and B6 represent boundaries between the droplet and the ambient environment both are set to room temperature *i.e.* 298.15 K.

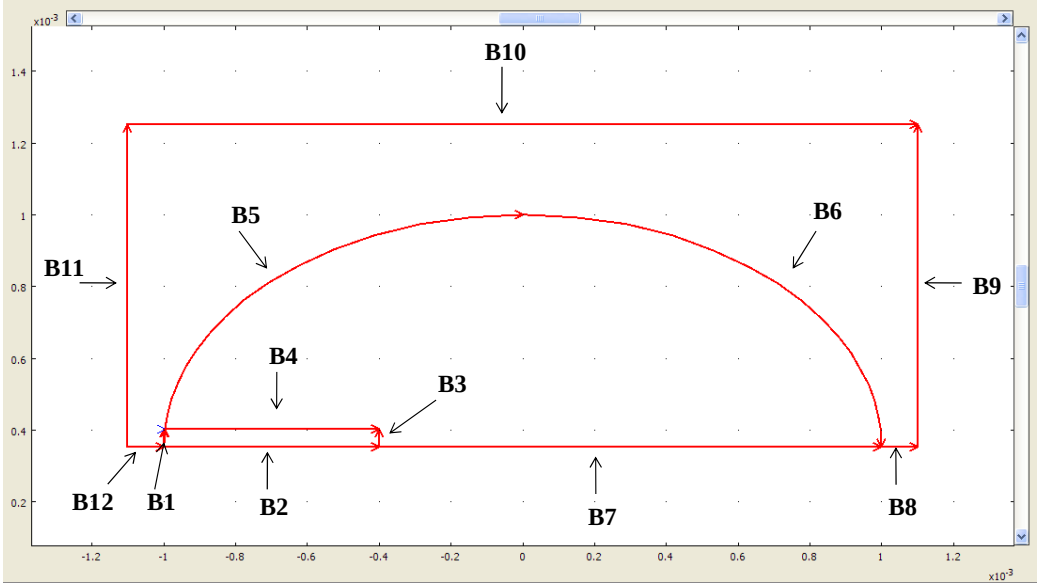

Figure 5.6: Various boundaries used for Convection and Conduction model in Comsol© software.

Table IV: Boundary conditions used for Convection and Conduction application mode in Comsol© simulation.

Settings	B1, B3, B4	B2, B7, B8, B9, B10, B11, B12	B5, B6
Boundary Condition	Temperature	Thermal Insulation	Temperature
Temperature	deltaT	-	298.15 K

5.4.2 Subdomain Settings

For the Convection and Conduction application mode subdomain S1 is defined as a mustard oil liquid droplet, S2 is defined as a polysilicon microheater and S3 is defined as room air as shown in Figure 5.7. Table V shows various settings used for defining thermal conductivity, density, heat capacity and velocity field for different subdomains.

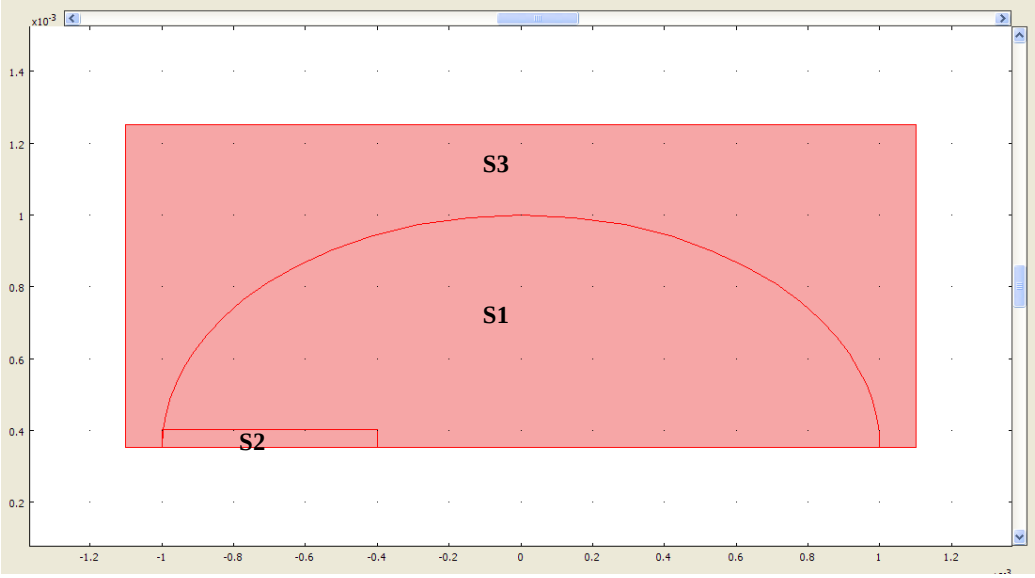

Figure 5.7: Subdomains used for Convection and Conduction application mode in Comsol© software.

Table V: Subdomain settings used for Convection and Conduction application mode in Comsol© simulation.

Settings	S1	S2	S3
Thermal Conductivity	k1	34 [W/(m*K)]	0.0257 [W/(m*K)]
Density	rho1	2320 [kg/m^3]	1.205[kg/m^3]
Heat Capacity	Cp1	678 [J/(kg*K)]	1012 [J/(kg*K)]
Velocity Field	u	0	0
Velocity Field	v	0	0

Furthermore, Table VI shows typical physical parameters used for mustard oil droplet during Comsol© simulation.

Table VI: Mustard oil physical parameters used for Comsol© simulation.

Parameter	Dynamic Viscosity (kg/(m.s))	Density (kg/m^3)	Thermal Conductivity (W/(mK))	Heat Capacity (J/(kg.K))	Thermal Expansion Coefficient (1/K)	Boiling Point (°C)
Value	**70**	**1020**	**0.15**	**2090**	**7e-4**	**151-153**

5.5 Weak Form, Boundary Model

This application mode is used to implement the condition that the shear stress is proportional to the temperature gradient on the surface. It defines the boundary conditions for liquid-air interface in our

model. Weak Form, Boundary application mode is used for models with separate partial differential equations (PDEs) on boundaries, edges or points. In general, all models are first transformed to the weak solution form before solving. The advantage of using weak solution form is that it provides with the exact Jacobian necessary for fast convergence of strongly nonlinear problems.

5.5.1 Boundary Conditions

The different boundaries selected for correctly simulating the model are shown in Figure 5.8. Furthermore, Table VII demonstrates the different boundary types and boundary conditions used for implementing Weak Form, Boundary application mode. Equation 5.1 describes the forces that the Marangoni effect induces on the liquid-air interface in the droplet.

$$\eta \frac{\partial u}{\partial y} = \gamma \frac{\partial T}{\partial x} \tag{5.1}$$

where η is the liquid dynamic viscosity, u is the liquid velocity, γ is the temperature derivative of surface tension (N/(m·K)), T is the temperature and x, y are horizontal and vertical coordinates of droplet. This equation states that the shear stress on a liquid surface is proportional to the temperature gradient.

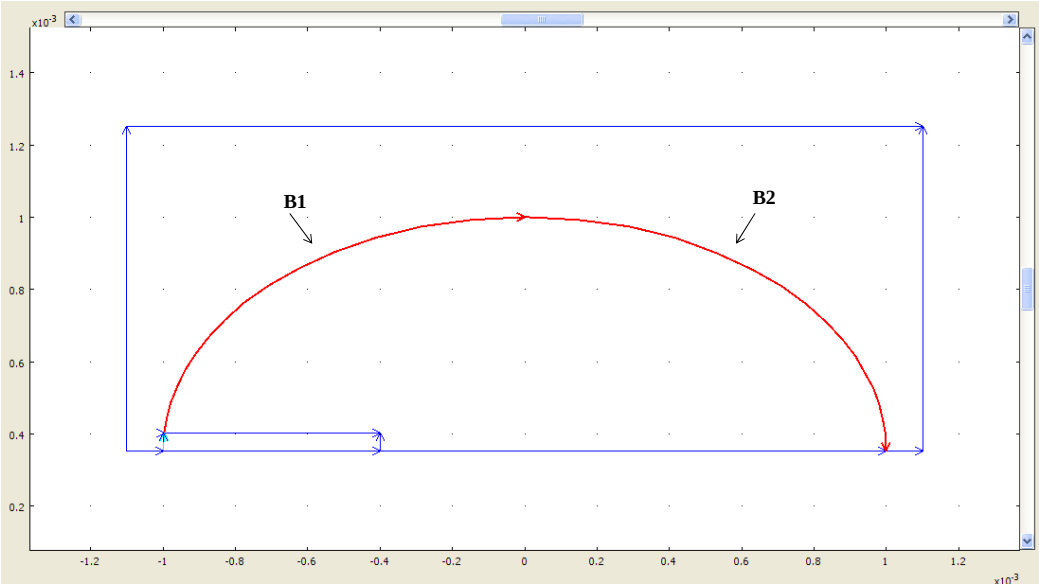

Figure 5.8: Various boundaries used for Weak Form, Boundary application mode in Comsol© software.

The boundary conditions B1 and B2 shown in Table VII are used to implement eq. (5.1). Meanwhile, there is no subdomain setting for this application mode as it only implements the liquid-air interface.

Table VII: Boundary conditions used for Weak Form, Boundary application mode in Comsol© simulation.

Settings	B1, B2
Weak Term	lm_test * (eta1 * uy – gamma * Tx) + u_test * lm

5.6 Simulation Results

When a temperature difference (ΔT) of 110 K was applied to the microdroplet using a microheater, surface tension gradient causes liquid to flow inside the droplet. Effectively that accounts for a temperature difference between the left and right side of the droplet. Two kind of liquid flows can be seen from Figure 5.9: liquid moving in counter-clockwise direction with higher velocity vectors and liquid flowing in clockwise direction with lower velocity vectors. This demonstrates that higher temperature difference causes higher surface tension gradient, causing liquid to move faster and thereby changing the droplet shape. Additionally, as can be seen from Figure 5.9, liquid velocity vectors inside the droplet are highest near the liquid-air interface, closer to the surface of the droplet. This is self-explanatory, as air is much colder due to room temperature causing a large surface tension gradient near liquid-air interface. This effect further enhances micro-object tilting and movement on top of the droplet.

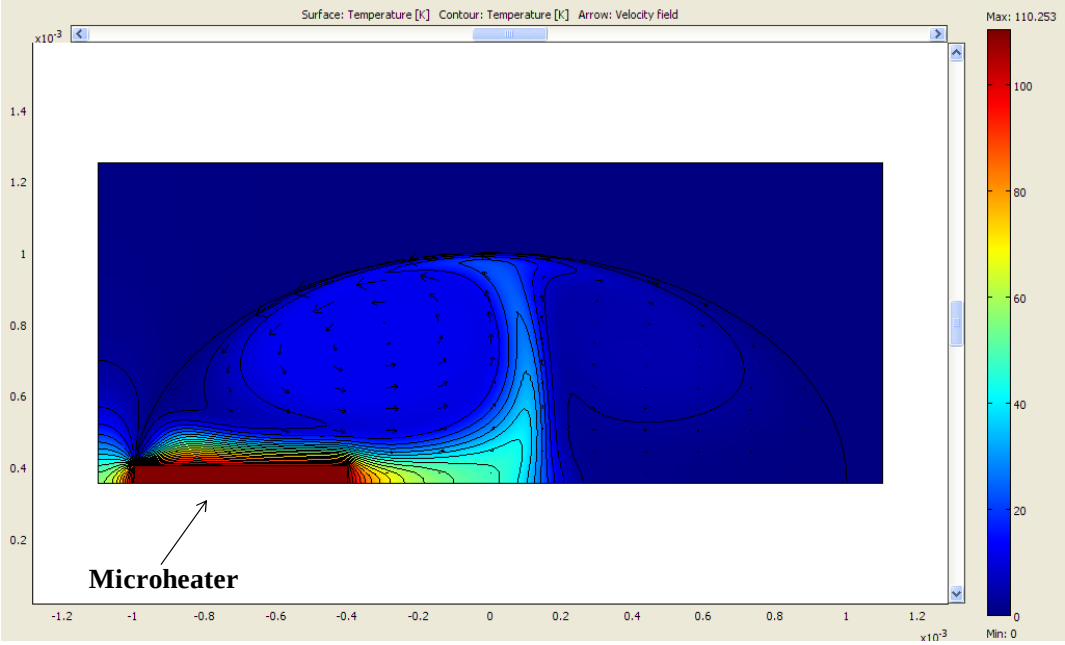

Figure 5.9: Thermocapillary effect causing liquid flow inside the droplet when a 110 K temperature difference was generated at left and right end of the droplet. Higher velocity vectors in counter-clockwise direction and lower velocity vectors in clockwise direction can be seen from the image. Simulation performed using Comsol© software.

Table VIII shows the maximum velocity in the *x* and *y* directions inside the droplet. Furthermore, low Reynolds number confirms a laminar flow inside the droplet.

Table VIII: Liquid velocity inside the droplet.

Parameter	Maximum x-velocity (mm/s)	Maximum y-velocity (mm/s)	Reynolds Number
Value	**38.9**	**33.1**	**4.4e-5**

----------x----------x----------x----------

6 Fabrication

6.1 Device Fabrication

The process flow for device fabrication is based on the RIT CMOS/MEMS processes [30-31] with necessary modifications, and it is illustrated in Figure 6.1. A total of four masks are needed for fabricating the device namely: Poly, Contact, Metal and Teflon. Device fabrication starts with the thermal growth of a 0.5 μm thick oxide layer, on top of a 500 μm silicon wafer. A 0.6 μm thick polysilicon layer is then deposited using LPCVD at 610 °C. Phosphorous-doped spin-on-glass (N-250) is coated, followed by thermal diffusion to increase the conductivity of the polysilicon layer. The first mask (Poly) is used to define the microheaters using photolithography and RIE dry etching. The poly microheaters are then partially oxidized at 1000 °C in dry oxygen ambient. The resistance of each microheater is measured using a multimeter and found to be approximately 430 ± 5 Ω.

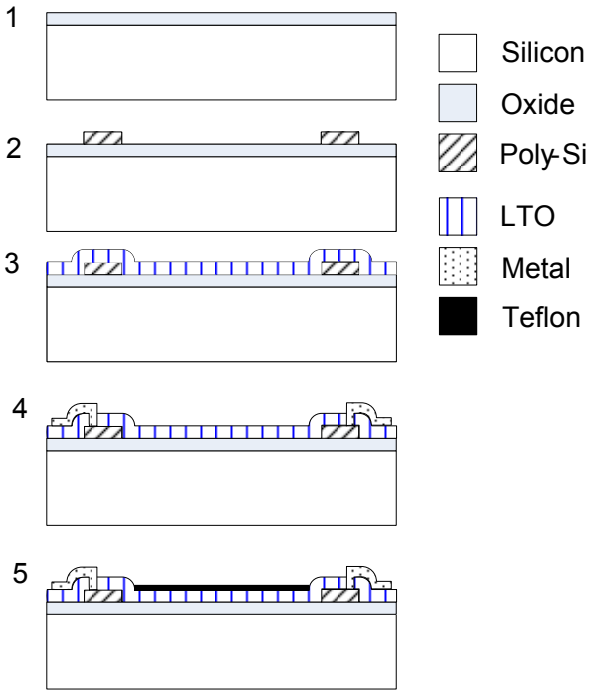

Figure 6.1: Process flow: (1) Thermal oxide is grown on top of silicon substrate. (2) Polysilicon layer is deposited and patterned to create microheaters. (3) LTO deposition. (4) LTO is etched for creating contact cuts. Subsequently, aluminum is sputtered and patterned for defining electrodes. (5) Finally, a Teflon layer is spin-coated and patterned.

A 1 μm thick LTO layer is then deposited using LPCVD. The second mask is then used to create contact cuts. Subsequently, an aluminum layer (1 μm) is sputtered and wet etched using the third mask to create contact pads for applying voltage to the microheaters. A Teflon© layer of 2000 Å thickness is spin-coated and lift-off to increase the hydrophobicity of the surface, which increased the contact angle of the oil droplet. The wafer is then diced into 4 x 4 mm^2 chips as shown in Figure 6.2. Additionally, Figure 6.3 (a, b) shows the close-up of two device chips. The complete process flow is discussed in Appendix B for interested readers.

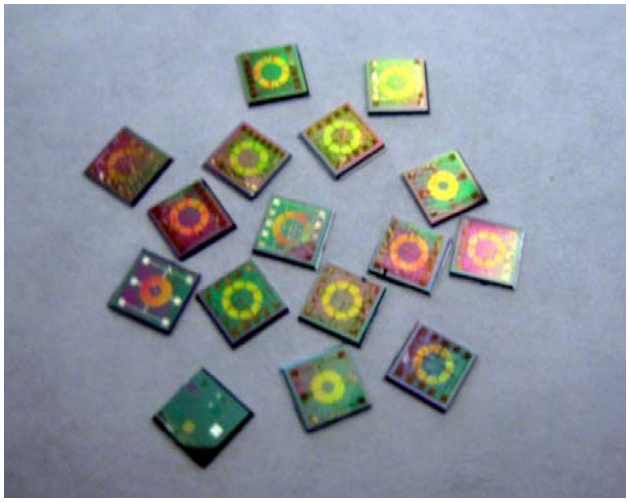

Figure 6.2: Different 4 x 4 mm^2 diced devices.

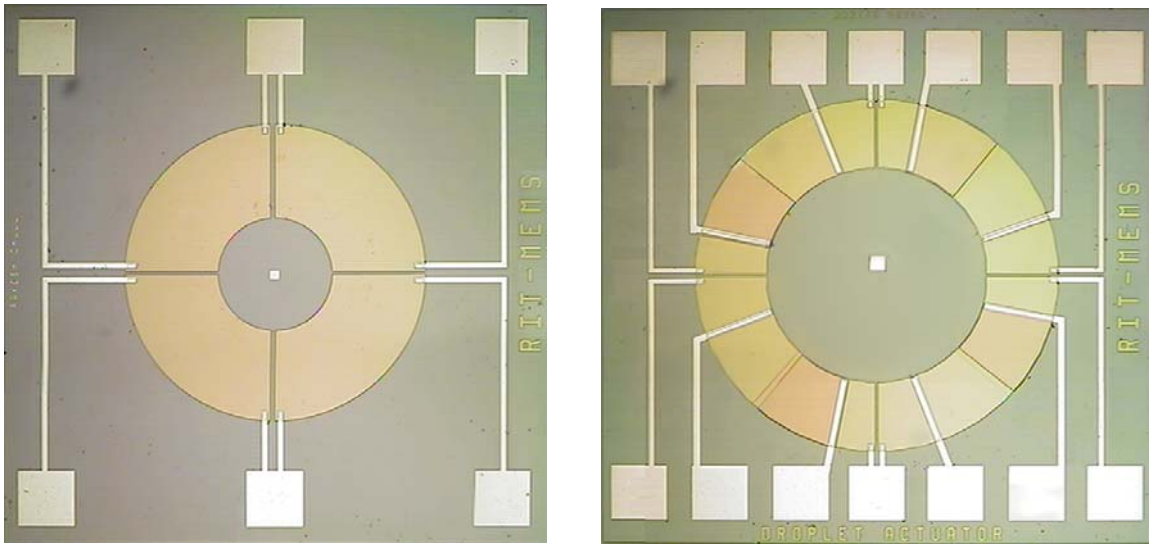

Figure 6.3: Device chips (a) Droplet actuator device used for micromirror tilting. (b) Droplet actuator device with buried p-n diodes for measuring chip temperature.

6.2 Micromirror Fabrication

The micromirrors were fabricated by depositing 0.8 μm thick aluminum layer on top of a transparent Polypropylene (PP) plastic sheet, using a thermal evaporator tool. The aluminum-coated plastic sheet was then cut into various-sized micromirrors using a fine scissor. The different size micromirrors are shown in Figure 6.4. Plastic micromirrors were used instead of silicon micromirrors, as they are more stable on top of a droplet due to their light weight. Additionally, they are simple, cost-effective and quick to fabricate compared to silicon micromirrors. For our preliminary test, a 1 x 1 x 0.1 mm^3 micromirror was placed onto the droplet using a micromanipulator.

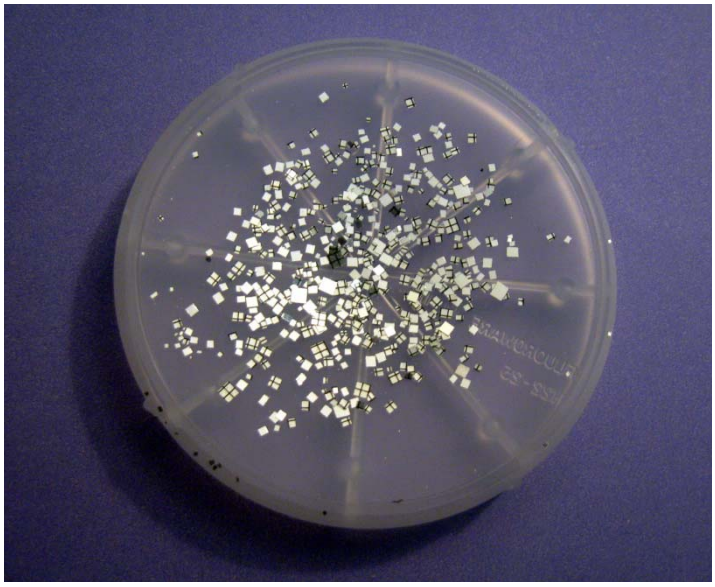

Figure 6.4: Different size aluminum coated micromirrors in a plastic dish.

6.3 PCB Fabrication

The fabrication process for making PCB boards is discussed below. The layout for PCB boards was designed using ExpressPCB software as shown in Figure 6.5. Subsequently, it was printed on a transparent plastic sheet and used as a mask. A copper board was first cleaned with fine steel wool followed by isopropanol, acetone and DI water cleansing [32]. HPR504 photoresist was then spin-coated at 1500 rpm for 60 seconds, followed by baking it at 110°C for 5 minutes. The copper board was then

flood exposed, using the PCB mask in a Karl-Suss aligner for ~10 sec, followed by treatment with CD-26 developer. Copper was then etched using a mixture of water, hydrogen peroxide (H_2O_2) and hydrogen chloride (HCl) in a 3:2:1 ratio. Finally, the copper board was cut into individual PCB boards using a sharp blade.

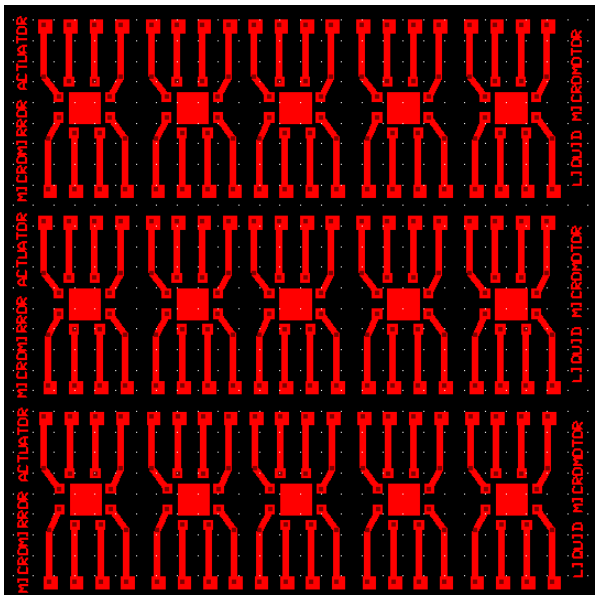

Figure 6.5: PCB board layout using ExpressPCB software.

----------x----------x----------x----------

7 Packaging

Proper packaging of the MEMS device is a critical step before any device testing can begin. Good packaging also ensures that the device performance is unaffected by external factors like vibration, temperature, humidity, etc. Micromirror actuation device packaging involved epoxy gluing of device chips in the center of a diced PCB board, using Hangar-9 6 minute epoxy as shown in Figure 7.1.

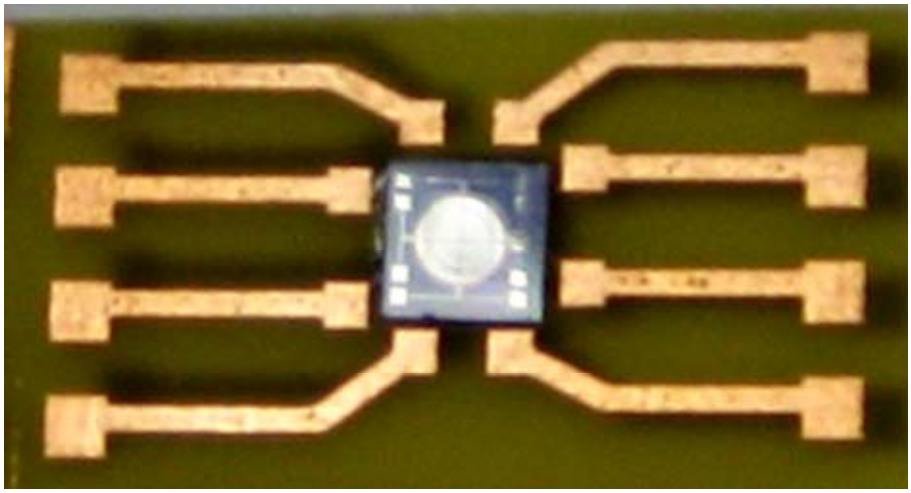

Figure 7.1: Device chip is epoxy glued in the center of the diced PCB board.

Subsequently, electrode pads on the device chip were wirebonded with PCB board electrodes using an ultrasonic wirebonding machine. To further increase the wirebond strength against shock and vibration, all of the wirebonds were encapsulated with a transparent epoxy glue (Hangar-9 6 minute epoxy), as shown in Figure 7.2. Afterwards, holes were drilled inside the PCB board and pin-strip headers (3M 929) were bonded to the PCB electrodes. This kind of packaging ensured the possibility of testing this device on a breadboard circuit. Consequently, a 1.2 μL mustard oil (allyl isothiocyanate) microdroplet, equivalent to a 2 mm base diameter, is placed in the center of the chip using a computer-controlled microsyringe (VCA Optima tool). Finally, a micro-manipulator is used to place the micromirror on top of the oil microdroplet. The complete packaged device with a micromirror onto a

microdroplet is shown in Figure 7.3. For size comparison purposes an individual chip, a packaged device and a penny are also shown in Figure 7.3. If required, microdroplet contamination can be minimized by covering the entire chip using a transparent plastic cover.

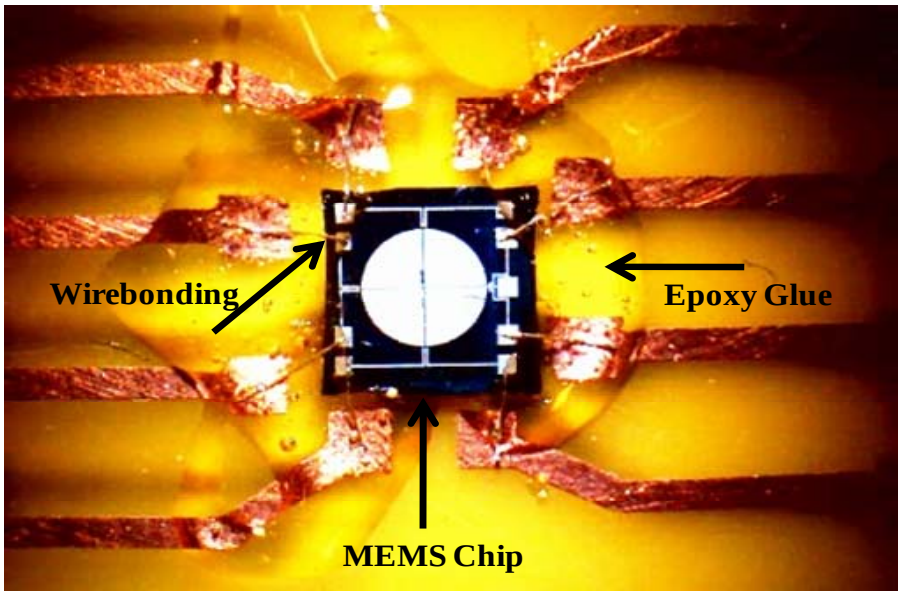

Figure 7.2: Device chip is wirebonded with PCB board electrodes. Wirebonds are encapsulated with epoxy glue to increase their strength against any shock and vibration.

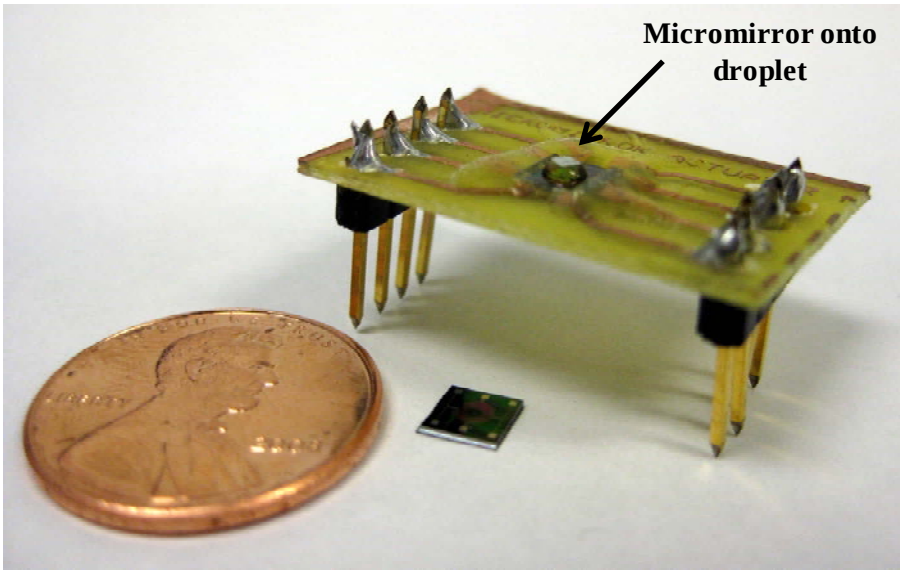

Figure 7.3: The complete packaged device with a micromirror onto a microdroplet. A penny is placed near the packaged device and device chip for size comparison.

----------x----------x----------x----------

8 Test Setups

8.1 Micromirror Tilting Test Setup

To find the relationship between the actuation voltage, the contact angles of the droplet, and the tilting angles of the micromirror, the measurement setup in Figure 8.1 was utilized. A CCD camera was used to capture video images of the droplet deformation and the micromirror actuation. A computer with software control enabled the optimization and configuration of the CCD camera and microsyringe systems. The control circuitry included employing a transistor switch and a function generator (Agilent 33250A) to apply pulsed DC voltages to the microheaters. The advancing and receding angles during microdroplet deformation were calculated using a goniometer (VCA Optima) with an accuracy of ± 0.1 degree.

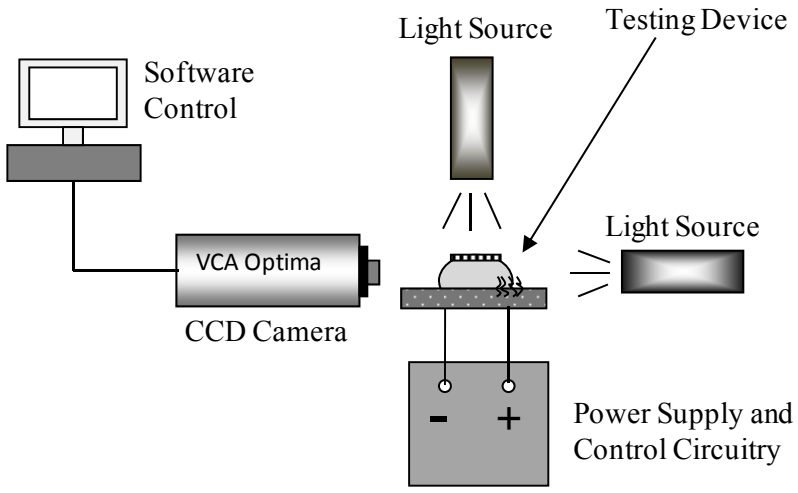

Figure 8.1: Schematic of the device test setup for measuring droplet advancing, receding angles and micromirror tilt angles.

The experimental setup of device testing is shown in Figure 8.2. A syringe containing mustard oil (yellowish liquid) was used to release microdroplet onto the chip surface. This phase of testing was performed before device packaging. As shown in the center of Figure 8.2, a device chip with a microdroplet was placed on a horizontal platform. Two probes were used to apply actuation voltages.

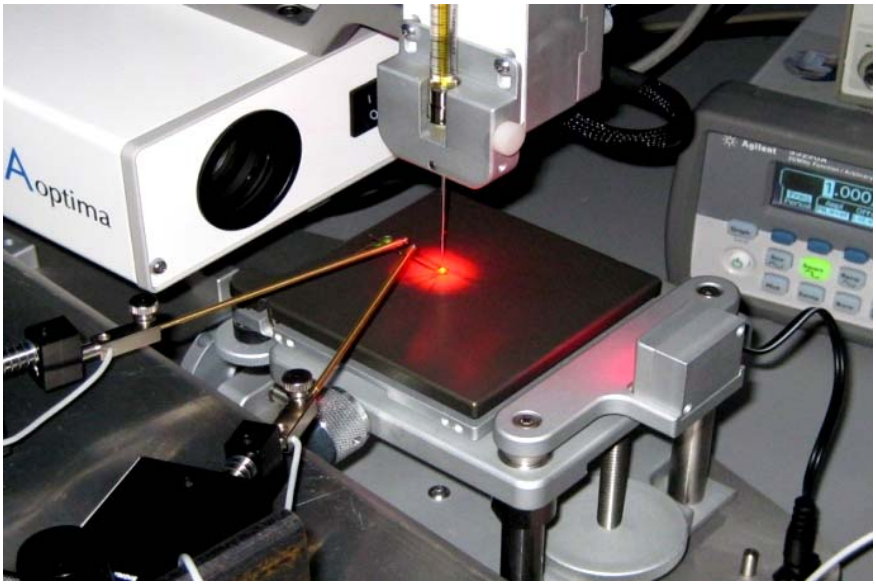

Figure 8.2: Experimental test setup for measuring advancing angle, receding angle, micromirror actuation and tilting.

8.2 Laser Test Setup

To test the application of micromirror actuation as a two-degrees-of-freedom (2-DOF) scanning micromirror, the setup shown in Figure 8.3 was employed. A HeNe laser of 633 nm wavelength and 0.8 mW power was used to demonstrate laser scanning. The control circuitry included a Complex Programmable Logic Device (CPLD, Xilinx CoolRunner-II CPLD board) and transistor switches to address the microheaters on the chip in a programmed sequence [33]. The actuation voltage applied to the four microheaters on the device chip in a programmed sequence (1, 2, 3, 4) is shown in Figure 8.4. As obvious from Figure 8.4, at any given time only a single microheater is in ON state. The Verilog code used to program CPLD board can be found in Appendix C for further details.

At first, the laser was focused onto the device micromirror after reflecting from a mirror as shown by dotted blue ray in Figure 8.3. The reflected laser image, reflected from the device micromirror was then captured on a flat screen, placed at a distance of 130 mm. A CCD camera was used to capture the video images of the laser scanning pattern. Meanwhile, different logic sequences were applied to demonstrate linear, square and circular laser scanning patterns.

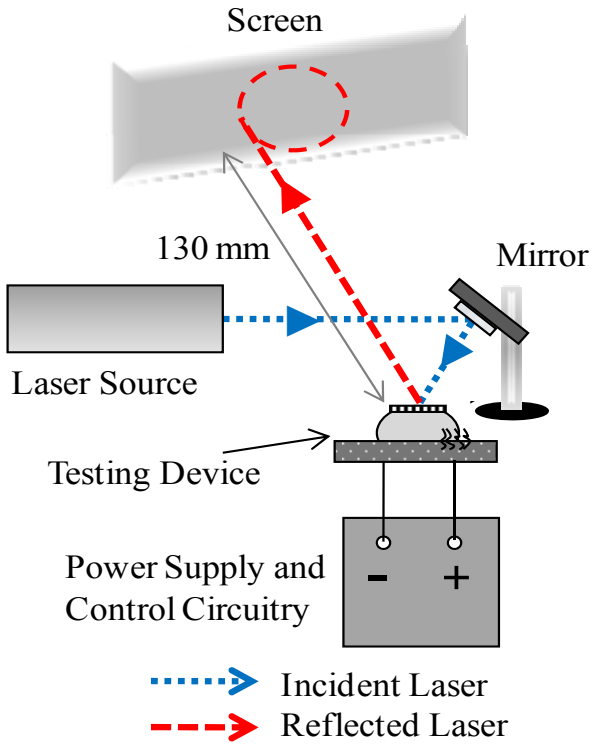

Figure 8.3: Schematic of the laser test setup to demonstrate a (2-DOF) scanning micromirror.

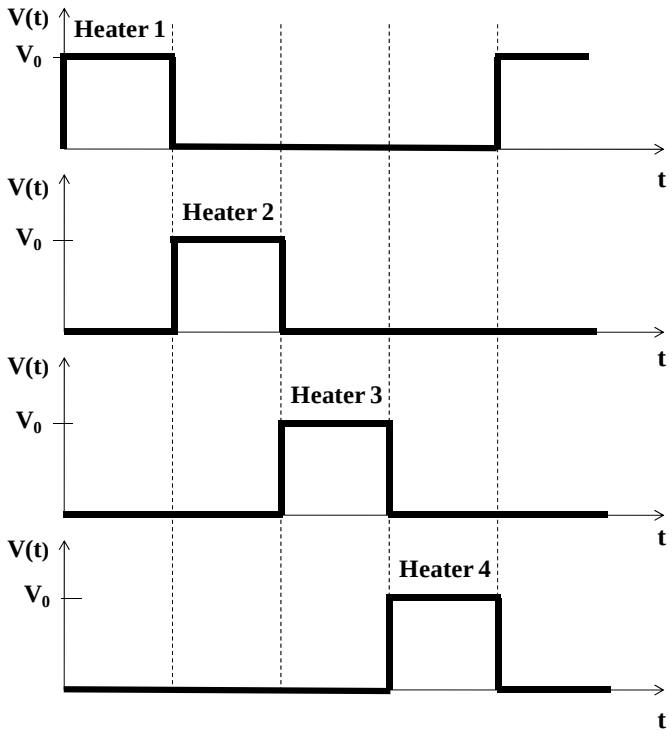

Figure 8.4: Actuation voltage applied to the four microheaters in a programmed sequence using a CPLD board to demonstrate a (2-DOF) scanning micromirror.

Furthermore, Figure 8.5(a, b) show the actual experimental setup used to test laser scanning on top of a shock- and vibration-free vacuum table. As shown in Figure 8.5(a, b) the device is placed onto a glass slide for the ease of applying actuation voltage.

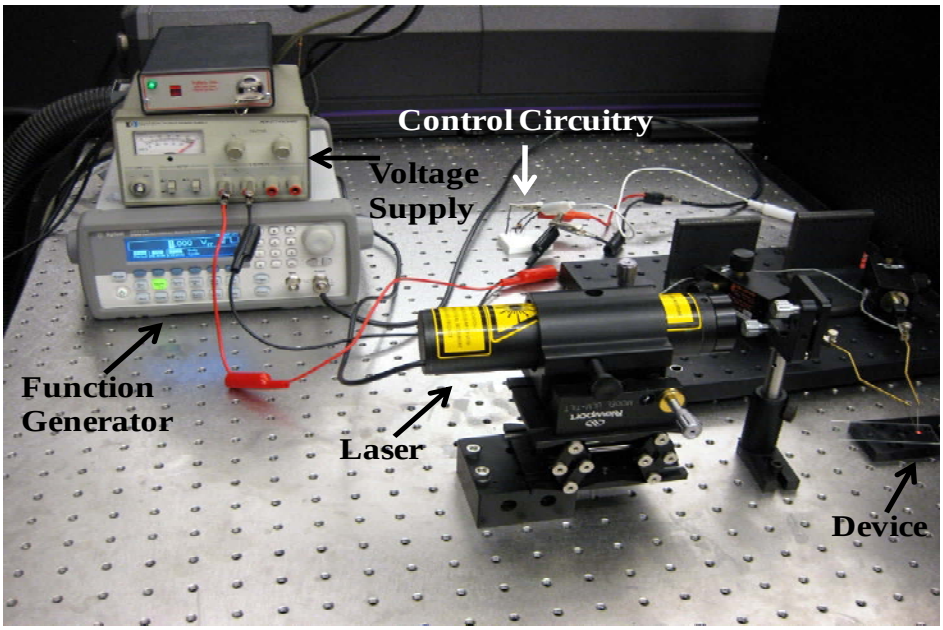

(a)

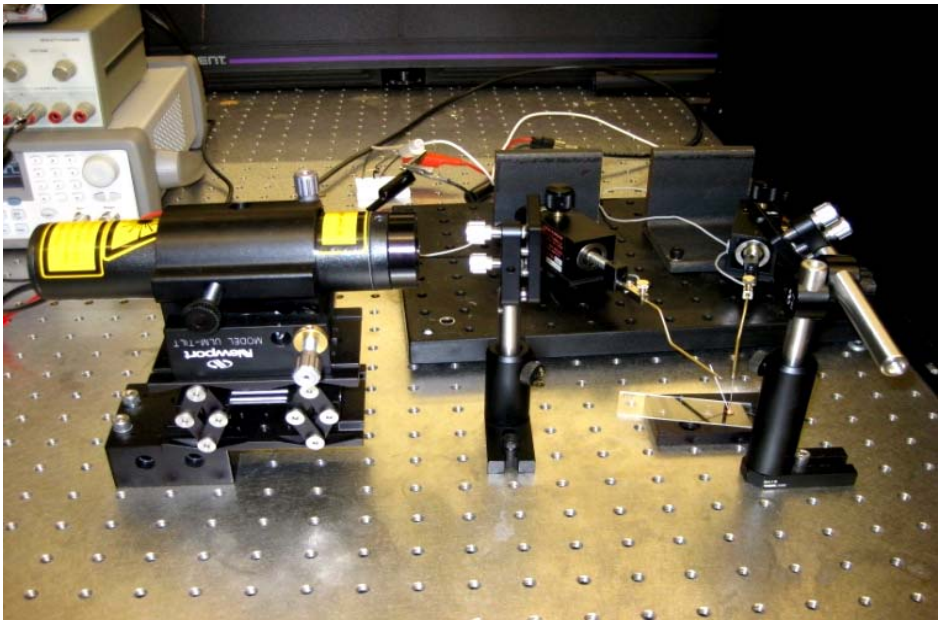

(b)

Figure 8.5: Laser experimental test setup to show the two-degrees-of-freedom (2-DOF) scanning micromirror: (a) Showing function generator, voltage supply, control circuitry and laser source. (b) Showing laser, mirror and device.

----------x----------x----------x----------

9 Results and Discussion

9.1 Thermocapillary Actuation

Initially, the device was tested to confirm thermocapillary actuation and droplet deformation. It is worth mentioning that all the tests during research were carried out in an ambient environment, at room temperature. A 1.2 μL mustard oil microdroplet was released in the center of chip with a computer-controlled microsyringe. The base diameter of the microdroplet was measured to be approximately 2 mm. Figure 9.1(a) shows the oil droplet without any voltage applied, hence no thermocapillary effect [34]. Similarly, Figure 9.1(b) shows the droplet actuation in the south-west direction when a 15 V, 1 Hz, 50 % duty cycle is applied to the first microheater. Reflection of light from the droplet surface clearly shows the change in droplet shape, thus confirming liquid flow due to Marangoni effect.

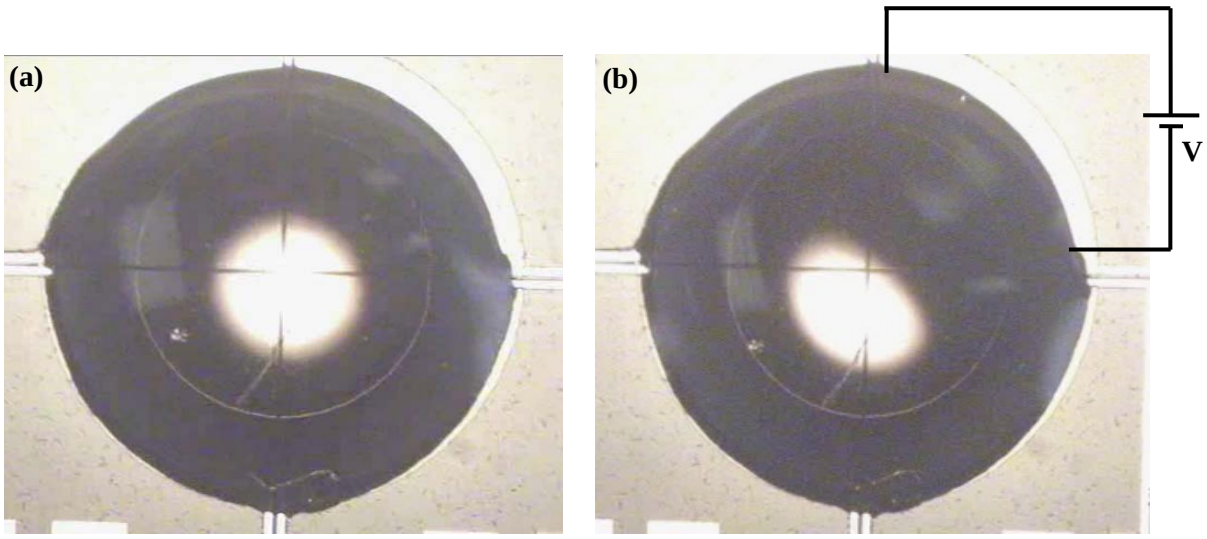

Figure 9.1: Reflection from the droplet surface, placed in the center of device without a micromirror: (a) without any actuation, and (b) when the voltage is applied to microheater 1 [34].

9.2 Micromirror Actuation and Tilting

The device is further tested with a micromirror on top of the droplet. For simplicity, a 1 x 1 x 0.1 mm^3 PP (Polypropylene) plastic sheet coated with aluminum was placed onto the droplet using a

micromanipulator. Different voltages were applied to deform the droplet and tilt the micromirror. The images in Figure 9.2 show the tilting of the micromirror [34-35]. As shown in Figure 9.2(a), a micromirror is resting on top of the droplet without any actuation voltage applied. The micromirror tilted 6.5° towards left when a 30 V, 1 Hz with 50% duty cycle voltage was applied to the polysilicon microheater using probes (as shown in Figure 9.2(b)). Furthermore, once the required micromirror tilt is obtained, the applied voltage needs to be decreased; otherwise it causes oil evaporation. This effect decreases the overall power requirements of the device. The typical current drawn by an individual microheater is 0.05 A with a total power requirement of 1.5 watts at 30 V actuation voltage.

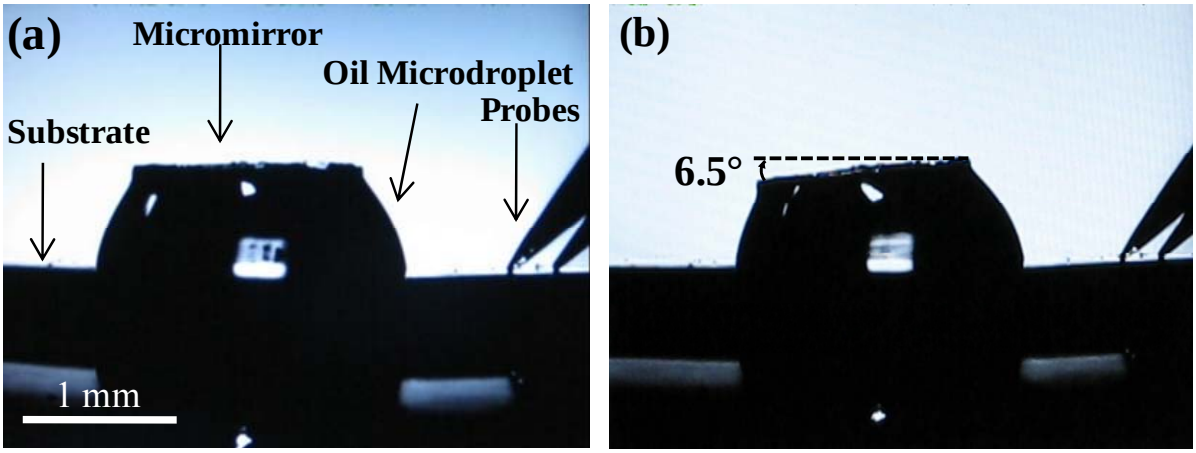

Figure 9.2: Micromirror actuation (a) Micromirror on top of the oil microdroplet @ 0V. (b) Microplate tilted 6.5° @ 30 V applied to one of the microheater [34-35].

Subsequently, different actuation voltages were applied and corresponding micromirror tilt angle, droplet advancing and receding angles were measured using the VCA Optima tool. Furthermore, Polytec Micro System Analyzer MSA-500 was used to confirm and analyze micromirror actuation at different applied voltage frequencies. Micromirror was found to be actuating even at 30 Hz frequency but with a lesser tilt angle. Since the liquid heating and convective flow inside the droplet is a relatively slow process it effectively decreases the Marangoni force on the micromirror at higher frequencies, causing a smaller micromirror tilt angle. Figure 9.3 shows the dependence of droplet tilt angle and contact angles with applied voltages [34-35]. The tilting angle of the micromirror was found to be almost linearly

dependent on the applied voltage. The black dotted line shows the linear match with the tilt angle data points. As the voltage was increased, the advancing *(θ_a)* angle of the droplet increased, effectively increasing the micromirror tilt angle. The receding angle *(θ_r)* was also found to be increasing slightly, instead of decreasing. This effect is possibly due to the presence of the micromirror on top of the droplet, which exerts a gravitational force on the droplet liquid. The advancing angle of the droplet increased from 79° to 86° whereas the receding angle increased from 78.9° to 81.8°.

It is interesting to note that the receding angle is also found to be increasing instead of decreasing. This is contrary to what can be expected from the thermocapillary effect theory in Chapter 3. This phenomenon can be explained by the fact that the theory described in Chapter 3 (Figure 3.1 and Figure 3.2) considers droplet actuation without any micromirror on top, when a temperature gradient is applied. However, when a micromirror is placed on the droplet it exerts a gravitational force on the droplet liquid. This downward force along with clockwise Marangoni flow causes receding angle to increase slightly. As the voltage is increased, the difference between advancing and receding angles increases, which correlates with the increasing tilt angle.

A maximum of 6.5° micromirror tilt angle at 30 V makes this technique easily integrable with current CMOS technology, thus providing an opportunity to fabricate a complete microsystem on a single chip. The device microheaters were found to be operating up to a maximum of 583 K after which they broke down due to excessive heat. Furthermore, the device was tested for up to 30 minutes at 30 V, 50% duty cycle, 1 Hz voltage without any oil evaporation. However, oil evaporation starts occuring if actuation voltage is increased above 30 V, thus limiting the device operation.

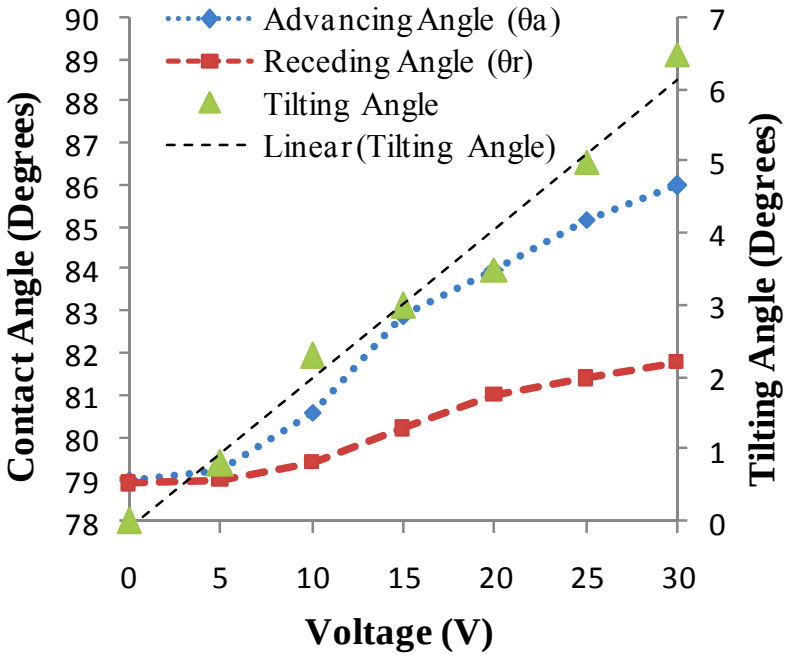

Figure 9.3: The dependence of the advancing and receding angles of the droplet, and the tilting angle of the micromirror at different applied voltages [34-35].

9.3 Laser Scanning

Figure 9.4(a) shows the linear scanning of laser beam when 30 V, 1 Hz actuation voltage was applied to one of the microheaters. A linear scan of 290 mm was obtained, which is quite large compared to other scanning results in literature. Subsequently, different actuation voltage sequences, implemented through the CPLD board, were applied to the microheaters to demonstrate different laser scanning patterns. Figure 9.4(b) shows the square-shape laser scanning when a 30 V, 1 Hz actuation voltage was applied to the microheaters in a 1, 2, 3, 4 cycle continuously using a CPLD board. In the case of Figure 9.4(a, b) the distance between the device micromirror and the capturing screen was set to be 2400 mm, which confirms large laser scanning distance. Consequently, microheaters were supplied with a 15 V actuation voltage at 10 Hz frequency in a continuous cyclic sequence (1, 2, 3, 4) using a CPLD board. As shown in Figure 9.4(c), a circular scanning pattern with a diameter of approximately 4 cm was obtained on the capturing screen, which confirms the two-degrees-of-freedom (2-DOF) micromirror scanning. Figure 9.4(c) was

obtained by superimposing three consecutive video frames of the scanning pattern using Image Stacker software (TawbaWare) [36].

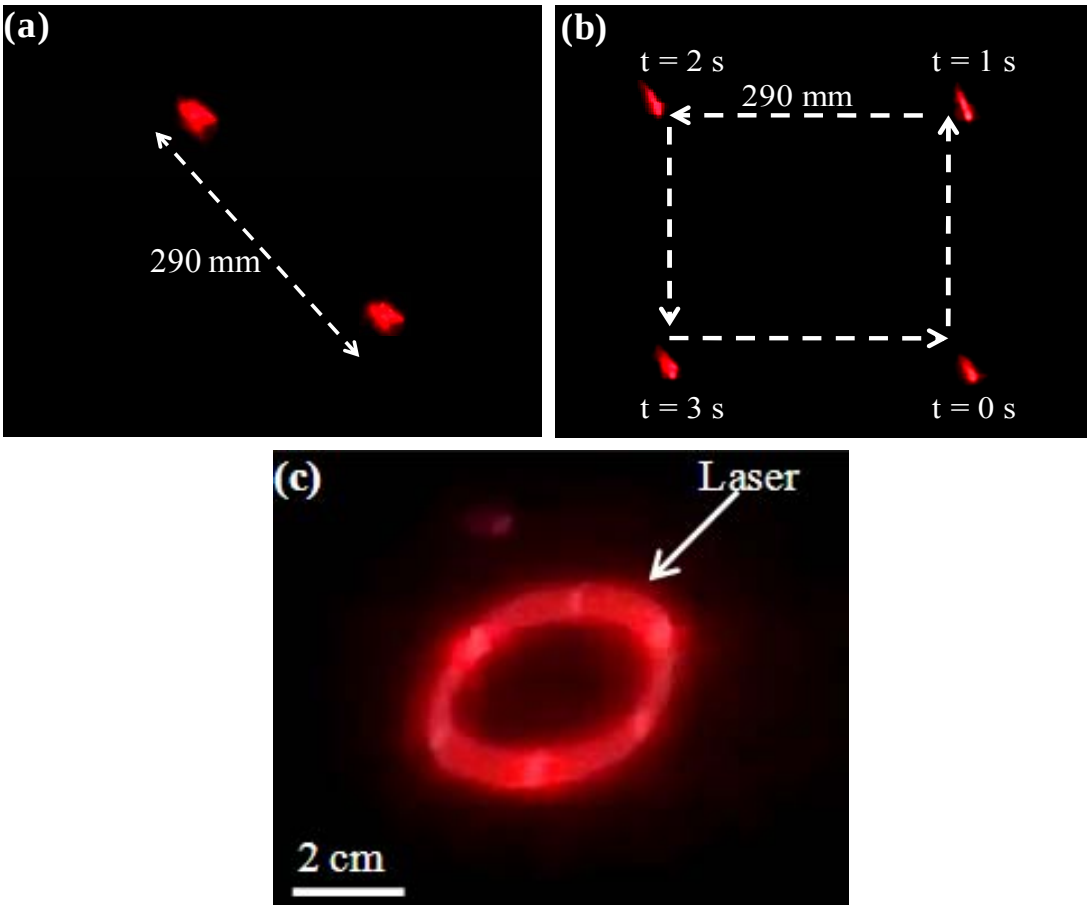

Figure 9.4: Different results obtained during the operation of the device. (a) Linear beam scanning @ 30 V, 1 Hz. (b) Square scanning of laser beam @ 30 V, 1 Hz. (c) Laser beam scanning a circle @ 15 V, 10 Hz actuation voltage.

However, an elliptical scanning pattern rather than a perfect circle was obtained. This can be explained by the fact that the camera was not at right angle to the capturing screen. Moreover, it may be possible that the mirror did not have a perfectly square shape. Since the applied voltage was just 15 V, the rotating angle of the micromirror was found to be approximately ± 3.7°. The frequency response of the device can be further improved by the miniaturization of the device, or by replacing the liquid with one having a higher surface tension and a lower viscosity [37].

----------x----------x----------x----------

10 Future Work

The performance of this device can be further improved by using a smaller droplet on top of smaller microheaters. Since the thermocapillary effect is based on convective flow of liquid, smaller oil droplet volume will ensure faster heat-up and flow of liquid inside the droplet, increasing the frequency response of the device.

Furthermore, a major improvement can be made by using a silicon micromirror instead of an aluminum-coated plastic micromirror. Oil heating by microheaters causes the heating of plastic micromirror, which causes micromirror to bend. This phenomenon modifies laser reflection from the micromirror, which changes the spot size of the laser on capturing screen. Since silicon has a relatively higher temperature coefficient of expansion compared to polypropylene plastic, using a silicon micromirror will minimize this problem and the same spot size can be expected during device operation. Additionally, to prevent oil contamination from dust particles and contaminants a transparent structure can be made around the microdroplet using polydimethlysiloxane (PDMS).

Another way to extend this research is by fabricating a 2 x 2 or 4 x 4 matrix of the devices and demonstrating different patterns – for example, writing a name or projecting a pattern. Moreover, the thermocapillary effect can also be utilized to demonstrate the operation of a liquid micromotor where a micro-object can be rotated on top of an oil microdroplet. The design for this kind of device is included in this research but device testing could not be finished.

----------x----------x----------x----------

11 Conclusion

Successful operation of a novel and simple way to actuate a micromirror on top of a mustard oil microdroplet is demonstrated. Thermocapillary effect in microdroplets is discussed with the effect of hysteresis on the stability of the droplet. Testing results confirm that devices can work at merely 10 V dc supply voltage. Increase in voltage increases the tilt angle of the micromirror with a maximum of 6.5° at 30 V, which is relatively improved compared to similar mechanisms reported in the literature. The small voltage requirements of the device allow it to be integrated with current CMOS processes, thus providing an opportunity for a complete microsystem on a single chip.

Device operational voltage and the stability of the microdroplet-micromirror system will further improve with the miniaturization of the device. Actuation of the micromirror on top of the microdroplet confirms that this device can be used for actuating micromirrors or micro-objects. Finally, a 2-degrees-of-freedom (2-DOF) scanning micromirror was demonstrated using a laser setup. Linear, square and circular laser scanning was demonstrated successfully, confirming possible applications in the field of scanning and display technology. Furthermore, the thermocapillary effect, which causes liquid to flow within the droplet from a hotter region towards a colder region and vice versa can be used judiciously for demonstrating a liquid micromotor.

----------x----------x----------x----------

References

[1] A. Werber and H. Zappe, "Thermo-pneumatically actuated, membrane-based micro-mirror devices", *Journal of Micromech. and Microeng.*, Oct 2006, pp. 2524-2531.

[2] Y. Yoshihata, N. B. Khiem, A. Takei, E. Iwase, K. Matsumoto and I. Shimoyama, "Scanning micromirror using deformation of a Parylene-encapsulated liquid structure", in *Proc. IEEE MEMS Conference*, Tucson, AZ, USA, Jan 2008, pp. 770-773.

[3] D. Elata and R. Mahameed, "A temperature-gradient driven micromirror with large angles and high frequencies", in *Proc. IEEE MEMS Conference, Istanbul*, Turkey, Jan 2006, pp. 850-853.

[4] U. Krishnamoorthy, D. Lee and O. Solgaard, "Self-Aligned Vertical Electrostatic Combdrives for Micromirror Actuation", *Journal of MEMS*, Aug. 2003, vol. 12, no. 4, pp. 458-464.

[5] D. Hah, P. R. Patterson, H. D. Nguyen, H. Toshiyoshi and M. C. Wu, "Surface- and bulk-micromachined two-dimensional scanner driven by angular vertical comb actuators", *Journal of MEMS*, Dec. 2005, vol. 10, no. 3, pp. 505-513.

[6] W. Piyawattanametha, R. P. J. Barretto, T. H. Ko, B. A. Flusberg, E. D. Cocker, H. J. Ra, D. S. Lee, O. Solgaard and M. J. Schnitzer, " Fast-scanning two-photon fluorescence imaging based on a microelectromechanical systems two- dimensional scanning mirror", *Opt. Lett.*, July 2006, vol. 31, no. 13, pp. 2018-2020.

[7] Y. Yee, H. J. Nam, S. H. Lee, J. U. Bu and J. W. Lee, "PZT actuated micromirror for fine-tracking mechanism of high-density optical data storage", *Sensors and Actuators a-Physical*, March 2001, vol. 89, no. 1-2, 166-173.

[8] A. Jain, A. Kopa, Y. T. Pan, G. K. Fedder and H. K. Xie, "A two-axis electrothermal micromirror for endoscopic optical coherence tomography", *Journal of Selected Topics in Quantum Electronics*, May-June 2004, vol. 10, no. 3, pp. 636-642.

[9] J. J. Bernstein, W. P. Taylor, J. D. Brazzle, C. J. Corcoran, G. Kirkos, J. E. Odhner, A. Pareek, M. Waelti and M. Zai, "Electromagnetically actuated mirror arrays for use in 3-D optical switching applications", *Journal of MEMS*, June 2004, vol. 13, no. 3, pp. 526-535.

[10] A. D. Yalcinkaya, H. Urey, D. Brown, T. Montague and R. Sprague, "Two-axis electromagnetic microscanner for high resolution displays", *Journal of MEMS*, Aug. 2006, vol. 15, no. 4, pp. 786-794.

[11] C. H. Ji, M. Choi, S. C. Kim, K. C. Song, J. U. Bu and H. J. Nam, "Electromagnetic two-dimensional scanner using radial magnetic field", *Journal of MEMS*, Aug. 2007, vol. 16, no. 4, pp. 989-996.

[12] H. Zeng, A. D. Feinerman, Z. Wan and P. R. Patel, "Piston-Motion Micromirror Based on Electrowetting of Liquid Metals", *Journal of MEMS*, April 2005, vol. 14, no. 2, pp. 285-293.

[13] S. K. Cho, Y. J. Zhao and C. J. Kim, "Concentration and binary separation of micro particles for droplet-based digital microfluidics", *Lab on a Chip*, 2007, vol. 7, no. 4, pp. 490-498.

[14] S. K. Cho, H. Moon and C. J. Kim, "Creating, transporting, cutting, and merging liquid droplets by electrowetting-based actuation for digital microfluidic circuits", *Journal of MEMS*, Feb. 2003, vol. 12, no. 1, pp. 70-80.

[15] P. Paik, V. K. Pamula, M. G. Pollack and R. B. Fair, "Rapid droplet mixers for digital microfluidic systems", *Lab on a Chip*, 2003, vol. 3, no. 1, pp. 28-33.

[16] M. A. Burns, B. N. Johnson, S. N. Brahmasandra, K. Handique, J. R. Webster, M. Krishnan, T. S. Sammarco, P. M. Man, D. Jones, D. Heldsinger, C. H. Mastrangelo and D. T. Burke, "An Integrated Nanoliter DNA Analysis Device", *Science*, Oct. 1998, vol. 282, no. 5388, pp. 484-487.

[17] A. A. Darhuber, J. P. Valentino, S. M. Troian and S. Wagner, "Thermocapillary actuation of droplets on chemically patterned surfaces by programmable microheater arrays", *Journal of MEMS,* Dec 2003, vol. 12, pp. 873-879.

[18] Z. Jiao, X. Huang, N. T. Nguyen and P. Abgrall, "Thermocapillary actuation of droplet in a planar microchannel", in *Journal of Microfluidics and Nanofluidics,* Aug 2008, vol. 5, no. 2, pp. 205-214.

[19] TI's Digital Micromirror Devices, "http://en.wikipedia.org/wiki/Digital_micromirror_device".

[20] TI's Digital Light Processing Technology, "http://www.dlp.com/default.aspx".

[21] DMD pixel exploded view, "http://www.yourdictionary.com/computer/dlp".

[22] DMD micromirror actuation, "http://www.opticalsciences.com/dmd.html".

[23] DLP projector operation, "http://hd.engadget.com/2005/10/22/hdtv-defined/".

[24] H. Kang and J. Kim, "EWOD (Electrowetting-on-dielectric) actuated optical micromirror", in *Proc. IEEE MEMS Conference*, Istanbul, Turkey, Jan 2006, pp. 742-745.

[25] J. Berthier, Microdrops and Digital Microfluidics (William Andrew Publishing 2008).

[26] J. Z. Chen, S. M. Troian, A. A. Darhuber and S. Wagner, "Effect of contact angle hysteresis on thermocapillary droplet actuation", *Journal of Applied Physics*, Dec 2004, vol. 97, no. 1, pp. 014906.

[27] Mustard oil properties, "http://msds.chem.ox.ac.uk/AL/allyl_isothiocyanate.html".

[28] J. B. Brzoska, F. Brochard-Wyart and F. Rondelez, "Motions of droplets on hydrophobic model surfaces induced by thermal gradients" *Langmuir*, 1993, vol. 9, pp. 2220.

[29] Z J Jiao, X Y Huang and N-T Nguyen, "Manipulation of a droplet in a planar channel by periodic thermocapillary actuation", *J. Micromech. Microeng.*, vol. 18, pp. 450270-9.

[30] Dr. Lynn Fuller's RIT MEMS bulk and surface micromachining process lecture notes, "http://people.rit.edu/lffeee/MEM_BULK_20082_Design_Project_Preview.pdf".

[31] Dr. Lynn Fuller's RIT CMOS process, "http://people.rit.edu/lffeee/cmos2009.pdf".

[32] Dr. Lynn Fuller's copper board packaging, "http://people.rit.edu/lffeee/RIT_Package.pdf".

[33] Xilinx CoolRunner-II CPLD boards, "http://www.xilinx.com/products/coolrunner2/index.htm".

[34] R. K. Dhull, I. Puchades, L. Fuller and Y.-W. Lu, *in Proc. of IEEE MEMS 2009*, Sorrento, Italy, Jan 2009, pp. 995-998.

[35] Y. W. Lu and R. Dhull, "Micromirror actuation using thermocapillary effect", *2nd ASME Micro/Nanoscale Heat & Mass Transfer International Conference*, Shanghai, China, Dec 2009.

[36] Image stacker software, "http://www.tawbaware.com/imgstack.htm".

[37] Z. Wan, H. Zeng and A. Feinerman, "Reversible electrowetting of liquid-metal droplet", *Transactions of the ASME*, April 2007, vol. 129, pp. 388-394.

Appendix A

Contact Angle Measurement

Two different methods commonly used to accurately measure the advancing and receding angles of an actuating microdroplet on a surface are discussed in this section.

A.1. Method 1

This method measures the advancing (θ_a) and receding (θ_r) angles of a microdroplet by continuously releasing and sucking liquid from a computer-controlled microsyringe. For our case, microdroplet contact angles are measured on a horizontal flat Teflon surface. For measuring advancing angle, liquid is released continuously at a constant rate from a microsyringe as shown in Figure A1(a). The images of angles thus formed by the droplet with the horizontal surface were captured using an built-in a CCD camera inside VCA Optima tool. Finally, the advancing angle was measured using VCA Optima software. Similarly, droplet receding angle can be measured by sucking the liquid droplet inside the microsyringe continuously at a constant rate as shown in Figure A1(b). The angle between droplet and flat Teflon surface thus formed will determine the receding contact angle.

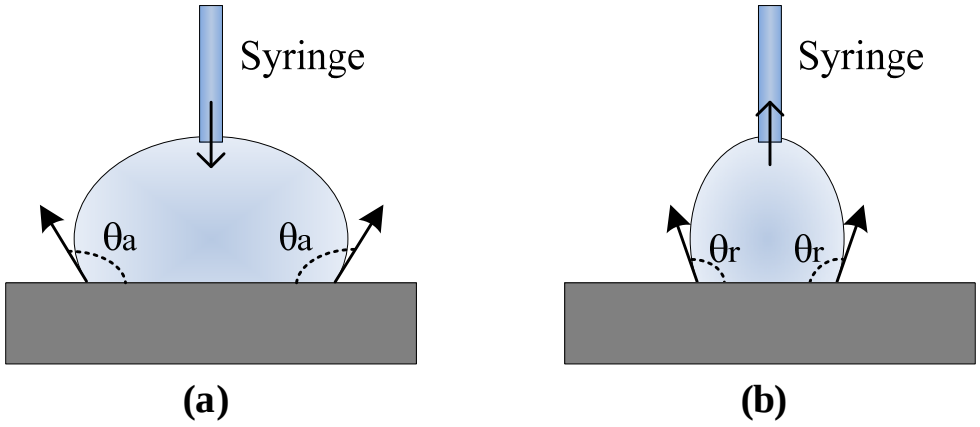

Figure A1: Contact angle measurement (a) Advancing angle is measured when liquid is moved out of the microsyringe. (b) Receding angle is measured when liquid is moved inside the microsyringe.

A.2. Method 2

The second method measured contact angles by employing a tilted surface, which causes liquid droplet to deform under the influence of gravity. To measure the advancing and receding angles accurately, a droplet is placed on a flat surface, which is gradually tilted to the maximum tilt angle where droplet starts moving. The angles thus formed by the droplet with the surface are advancing and receding angles as shown in Figure A2. A VCA Optima tool can be used to capture images of the droplet deformation and to measure contact angles.

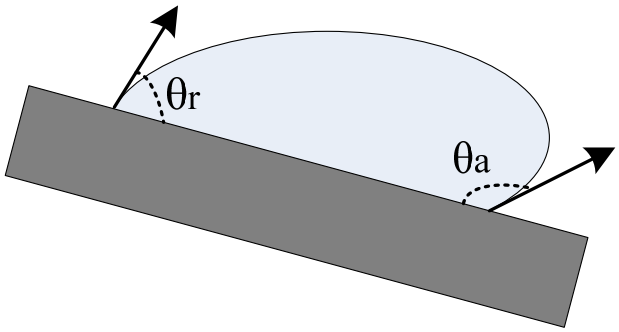

Figure A2: The dependence of the advancing angle and receding angle of the droplet, and the tilting angle of the microplate at different applied voltages.

Appendix B

Process Flow

The process flow used for fabricating micromirror actuation device was adapted from Dr. Lynn Fuller's RIT MEMS bulk and surface micromachining process. A total of four masks are required namely: Poly, Contact Cut, Metal and Teflon.

Step	Instructions
1	Obtain qty 3, 4" n-type wafers
2	RCA Clean 10 min SC1, 15:3:1 H20:H2O2:NH4OH 5 min DI water rinse 60 sec 50:1 HF 5 min DI water rinse 10 min SC2 15:3:1 H2O:H2O2:HCL 5 min DI water rinse SRD
3	Grow 5000Å oxide recipe 350 Enter Nanospec thickness: 1_____, 2_____, 3_____, 4_____, 5_____
4	Deposit 6000 Å poly LPCVD Use 610C Poly recipe Soak time from log sheet= _____

	Enter Nanospec thickness: 1_____, 2_____, 3_____, 4_____, 5_____
5	Spin on Glass, N-250 3000 rpm 30sec Blue oven bake at 200C for 20 minutes in air ambient
6	Poly Diffusion, Recipe 120 15 min in N2 at 1000C
7	Etch SOG 7 min 5.2:1 BOE
8	4 pt Probe on edge of wafer with manual 4pt probe Voltage= _____, Current=_____ Rs= _____ ohm/sq
9	Photo 3, Poly Coat in wafer track – recipe 1 (HMDS vapor prime, coat S1813 resist_4500rpm_60sec, softbake_90C_60sec) Expose using KS55 aligner with 14 sec exposure.

	Develop in wafer track – recipe 1 (peb_115C_60sec, develop_CD26_50sec,hard_bake_125C_60sec) Enter minimum resolution line: _____ um **Alternate:** Hand coat with CEE spinner – Dehydration bake_120C_60sec, HMDS spin_4500rpm_60sec, coat S1813 resist_4500_rpm_60sec, softbake_90C_60sec) Expose using KS55 aligner with 14 sec exposure. Hand develop (peb_115C_60sec, develop_CD26_50sec, DI water rinse and air-gun dry, hard_bake_125C_60sec) Enter minimum resolution line: _____ um
10	Etch poly, LAM490 Use FACPOLY recipe, endpoint detection may not work due to smaller 4" wafer area. (Expect ~1'05'') Time/wafer = _____

11	Strip Resist 5 min solvent clean + 10 min DI water rinse + SRD
12	RCA Clean 10 min SC1, 15:3:1 H20:H2O2:NH4OH 5 min DI water rinse 60 sec 50:1 HF 5 min DI water rinse 10 min SC2 15:3:1 H2O:H2O2:HCL 5 min DI water rinse SRD
13	Oxidize Poly Recipe 250 Soak: 54min dryO2 at 1000C Enter Nanospec thickness: 1_____, 2_____, 3_____, 4_____, 5_____
14	Deposit 1µm LTO LPCVD 410C LTO, include bare-Si dummy wafer Soak time from log sheet= _____

	Enter Nanospec thickness of bare-Si dummy wafer: 1_____, 2_____, 3_____, 4_____, 5_____
15	Photo 4, Contact Cut Coat in wafer track – recipe 1 (HMDS vapor prime, coat S1813 resist_4500rpm_60sec, softbake_90C_60sec) Expose using KS55 aligner with 14 sec exposure. Develop in wafer track – recipe 1 (peb_115C_60sec, develop_CD26_50sec,hard_bake_125C_60sec) Enter minimum resolution line: _____ um **Alternate:** Hand coat with CEE spinner – Dehydration bake_120C_60sec, HMDS spin_4500rpm_60sec, coat S1813 resist_4500_rpm_60sec, softbake_90C_60sec) Expose using KS55 aligner with 14 sec exposure. Hand develop (peb_115C_60sec, develop_CD26_50sec, DI water rinse and air-gun dry, hard_bake_125C_60sec) Enter minimum resolution line: _____ um

16	Etch Contact Cut in BOE, Rinse, SRD 5.2:1 BOE, determine etch time based on LTO thickens. Etch rate is ~2000Å/min Enter etch time: _____ min Enter approximate delta CD after etch. ____ um
17	Strip Resist 5 min solvent clean + 10 min DI water rinse + SRD
18	RCA Clean, include extra HF 10 min SC1, 15:3:1 H20:H2O2:NH4OH 5 min DI water rinse 60 sec 50:1 HF 5 min DI water rinse 10 min SC2 15:3:1 H2O:H2O2:HCL 5 min DI water rinse 20 sec 50:1 HF 5 min DI water rinse SRD
19	Deposit Aluminum, 10,000Å Al/Si 8" target, 2000 Watts, Argon, 5 mTorr dep pressure

	Dep time from logsheets: _____ min (33min in 20062) Use dummy wafer with tape to measure step height. Alpha-step Al thickness = _____ Å
20	Photo 5, Metal Coat in wafer track – recipe 1 (HMDS vapor prime, coat S1813 resist_4500rpm_60sec, softbake_90C_60sec) Expose using KS55 aligner with 9 sec exposure Develop in wafer track – recipe 1 (peb_115C_60sec, develop_CD26_50sec,hard_bake_125C_60sec) Enter minimum resolution line: _____ um **Alternate:** Hand coat with CEE spinner – Dehydration bake_120C_60sec, HMDS spin_4500rpm_60sec, coat S1813 resist_4500_rpm_60sec, softbake_90C_60sec) Expose using KS55 aligner with 9 sec exposure Hand develop (peb_115C_60sec, develop_CD26_50sec, DI water rinse and air-gun dry, hard_bake_125C_60sec)

	Enter minimum resolution line: _____ um
21	Etch Aluminum, Wet Etch Use agitation or dunking technique to ensure that Al etches in smaller spaces. Time should be 4-5 minutes. Run one wafer first and inspect carefully, then the rest of wafers.
22	Spin-coat Teflon AF 1600 solution. 500 rpm for 10 sec, 2000 rpm for 30 sec. Bake at 150 °C for 10 minutes.
23	Spin-coat photoresist.
24	Photo step for clearing Teflon from top of electrodes.
25	Etch Teflon from top of electrodes.
26	Etch Resist.
27	Dice wafer.
28	Package devices on a PCB board for testing.
29	Place microdroplet and micromirror in the center of device.
30	Test devices.

Appendix C

Verilog Code for Xilinx CPLD Board

```
count :process (sclk_processing)
begin
if sdata_in = "00000001" then
 clk_divider <= "00000";
elsif (sclk_processing'event and sclk_processing='1') then
   if (clk_divider = "11101") then
      clk_divider <= (others=>'0');
    else
      clk_divider <= clk_divider + 1;
    end if;
end if;
end process count;
shift :process(sclk_processing, data_in)
begin
if data_in = "00000001" then
 temp (15 downto 0 ) <= ("0000000000000001");
elsif sclk_processing'event and sclk_processing = '1' then
 if clk_divider <= "01110" then
  temp(15  downto 0) <= temp(14 downto 0) & temp(15);
 elsif ("01111" <= clk_divider) then
  temp(15  downto 0) <=  temp(0) & temp(15 downto 1);
 end if;
end if;
end process shift;
```

```
sclk_processing <= clk_processing;

hex <= temp;
```